Low luminosity states of hte black hole candidate GX 339-4. I. ASCA and simultaneous radio/RXTE observations

Wilms, J.; Nowak, M.A.; Dove, J.B.; Fender, R.P.; Di Matteo, T.

Published in:
Astrophysical Journal

DOI:
10.1086/307622

THE ASTROPHYSICAL JOURNAL, 522:460–475, 1999 September 1

LOW-LUMINOSITY STATES OF THE BLACK HOLE CANDIDATE GX 339−4. I. *ASCA* AND SIMULTANEOUS RADIO/*RXTE* OBSERVATIONS

JÖRN WILMS,[1] MICHAEL A. NOWAK,[2] JAMES B. DOVE,[2,3] ROBERT P. FENDER,[4] AND TIZIANA DI MATTEO[5,6]

Received 1998 October 12; accepted 1999 April 14

ABSTRACT

We discuss a series of observations of the black hole candidate GX 339−4 in low-luminosity, spectrally hard states. We present spectral analysis of three separate archival *Advanced Satellite for Cosmology and Astrophysics* (*ASCA*) data sets and eight separate *Rossi X-Ray Timing Explorer* (*RXTE*) data sets. Three of the *RXTE* observations were strictly simultaneous with 843 MHz and 8.3–9.1 GHz radio observations. All of these observations have (3–9 keV) flux $\lesssim 10^{-9}$ ergs s^{-1} cm^{-2}. The *ASCA* data show evidence for an $\approx$6.4 keV Fe line with equivalent width $\approx$40 eV, as well as evidence for a soft excess that is well modeled by a power law plus a multicolor blackbody spectrum with peak temperature $\approx$150–200 eV. The *RXTE* data sets also show evidence of an Fe line with equivalent widths $\approx$20–140 eV. Reflection models show a hardening of the *RXTE* spectra with decreasing X-ray flux; however, these models do not exhibit evidence of a correlation between the photon index of the incident power law flux and the solid angle subtended by the reflector. "Sphere+disk" Comptonization models and advection-dominated accretion flow (ADAF) models also provide reasonable descriptions of the *RXTE* data. The former models yield coronal temperatures in the range 20–50 keV and optical depths of $\tau \approx 3$. The model fits to the X-ray data, however, do not simultaneously explain the observed radio properties. The most likely source of the radio flux is synchrotron emission from an extended outflow of size greater than $\mathcal{O}(10^7 GM/c^2)$.

Subject headings: binaries: close — black hole physics — radiation mechanisms: nonthermal — stars: individual (GX 339−4) — X-rays: stars

1. INTRODUCTION

The Galactic black hole candidate (BHC) GX 339−4 is unique among persistent sources in that it shows a wide variety of spectral states and transitions among these states. In presumed order of increasing bolometric luminosity, GX 339−4 exhibits a state with hard, power-law spectra ("off state:" Ilovaisky et al. 1986; "low state:" Grebenev et al. 1991); a soft state with no evidence of a power-law tail ("high state;" Grebenev et al. 1991); and a very bright, soft state with an extended power-law tail ("very high state;" Miyamoto et al. 1991). There also are apparently times when the flux is high but the spectrum is not as soft as in the high or very high state. Méndez & van der Klis (1997) refer to this as the "intermediate state." We also note that there is some evidence of overlap between the states. The broadband (*Granat* SIGMA) hard-state data presented by Grebenev et al. (1991) apparently represents a more luminous state than does the broadband soft-state data taken with the same instrument. (Miyamoto et al. 1995 has suggested the possibility of hysteresis in Galactic BHC state transitions.) Similarly diverse sets of states have been observed in X-ray transients such as Nova Muscae (Kitamoto et al. 1992; Miyamoto et al. 1994); however, GX 339−4 is closer to being a persistent source.

Although there have been a number of observations of GX 339−4 in the near-infrared and optical (Doxsey et al. 1979; Motch et al. 1983, 1985; Steiman-Cameron et al. 1990; Imamura et al. 1990; Cowley et al. 1991), including detection of a 14.8 hr periodicity in the optical (Callanan et al. 1991), there is no convincing mass function for the system. In the optical, the system is faint, variable ($M_V \approx$ 16–20), and reddened ($A_V = 3.5$). The physical source of the optical emission is unknown. It has been hypothesized that it is entirely dominated by the accretion disk, as the optical flux is apparently anticorrelated with the soft X-ray emission (Steiman-Cameron et al. 1990; Imamura et al. 1990). These properties of the emission have made it difficult to obtain a good distance measurement, with estimates ranging from 1.3 kpc (Predehl et al. 1991) to 8 kpc (Grindlay 1979), with many authors choosing 4 kpc (Doxsey et al. 1979; Cowley, Crampton, & Hutchings 1987). A careful study of these distance estimates is presented by Zdziarski et al. (1998), who argue for a distance of $\approx$4 kpc.

GX 339−4 also has been detected in the radio (Sood & Campell-Wilson 1994) and possibly even has exhibited extended emission (Fender et al. 1997). Within the hard state, the radio spectrum is flat/inverted with a spectral index of $\alpha = 0.1$–0.2 (Fender et al. 1997; Corbel et al. 1997), where the radio flux density $S_\nu \propto \nu^\alpha$. Furthermore, in this state the radio flux is correlated with the X-ray and gamma-ray fluxes (Hannikainnen et al. 1999), but the radio flux disappears as GX 339−4 transits to a higher X-ray flux/softer state (Fender et al. 1999), which is comparable to the behavior of Cyg X-1 (Pooley, Fender, & Brocksopp 1999).

During the *Rossi X-Ray Timing Explorer* (*RXTE*) Cycle 2 observing phase (1996 December–1998 February), we performed a series of eight *RXTE* observations of GX 339−4.

[1] Institut für Astronomie und Astrophysik, Abt. Astronomie, Waldhäuser Strasse 64, D-72076 Tübingen, Germany; wilms@astro.uni-tuebingen.de.

[2] JILA, University of Colorado, Campus Box 440, Boulder, CO 80309-0440; mnowak@rocinante.colorado.edu.

[3] Present address, CASA, University of Colorado, Campus 389, Boulder, CO 80309-0389; dove@casa.colorado.edu.

[4] Astronomical Institute Anton Pannekoek, University of Amsterdam, and Center for High-Energy Astrophysics, Kruislaan 403, 1098 SJ, Amsterdam, Netherlands; rpf@astro.uva.nl.

[5] Institute of Astronomy, Madingley Road, Cambridge CB3 OHA, UK; tiziana@ast.cam.ac.uk.

[6] *AXAF* Fellow; present address: Harvard -Smithsonian Center for Astrophysics, Cambridge, MA 01238; tdimatteo@cfa.harvard.edu.

TABLE 1

LOG OF THE *ASCA* OBSERVATIONS

Observation	Date	Integration Time (ks)	SIS0 (counts s^{-1})	3–9 keV Flux (10^{-9} ergs cm^{-2} s^{-1})
1	1994 Aug 24	15	3.6	0.11
2	1994 Sep 12	17	6.4	0.19
3	1995 Sep 8	30	17.5	0.63

NOTE.—All observations were taken in Bright 1-CCD mode. SIS0: filtered SIS0 count rate.

The first three observations were spaced a week apart from one another from 1997 February 4 to 1997 February 18. These three observations were scheduled to be simultaneous with 8.3–9.1 GHz radio observations that were conducted at the Australian Telescope Compact Array (ATCA). The results of the radio observations have been reported by Corbel et al. (1997). Additionally, three 843 MHz observations performed at the Molongolo Observatory Synthesis Telescope (MOST) and reported by Hannikainnen et al. (1999) are also simultaneous with these *RXTE* observations. This paper is structured as follows. We discuss the spectral analysis of archival *Advanced Satellite for Cosmology and Astrophysics* (*ASCA*) data in § 2. We look for evidence of Fe lines in the data and we characterize the soft ($\lesssim$1 keV) X-ray data. In § 3 we present the *RXTE* data. We first discuss the All Sky Monitor (ASM) data, and then we discuss the pointed observations. We perform spectral analysis much akin to that which we considered for Cyg X-1 (Dove et al. 1998). Here, however, we consider advection-dominated accretion flow (ADAF) models as well by using the models described by Di Matteo et al. (1999). We discuss the implications of the simultaneous radio data in § 4. In § 5 we discuss the implications of the X-ray observations for theoretical models. We summarize our results in § 6. We present timing analysis of the *RXTE* data in a companion paper (Nowak, Wilms, & Dove 1999, hereafter Paper II).

2. ARCHIVAL *ASCA* OBSERVATIONS

The *ASCA* archives contain four observations of the GX 339−4 region. A log of the observations is given in Table 1. In Appendix A, we describe the methods that we used to extract, filter, and analyze these *ASCA* observations. To the best of our knowledge, an analysis of these observations has not been published previously, except for a power spectrum for one of the observations (date not given; Dobrinskaya et al. 1997). The first of the observations (1993 September 16) did not detect the source, with the upper limit to the 3–9 keV flux being $\approx 10^{-12}$ ergs s^{-1} cm^2. As we will discuss below, the inferred 3–9 keV fluxes for the remaining three observations (Table 1) are lower by factors of 2–10 than the fluxes of the *RXTE* observations discussed in § 3.

We chose to fit the *ASCA* data with a phenomenological model consisting of a multicolor blackbody spectrum plus a broken power law, considered with and without a narrow Gaussian line at $\approx$6.4 keV. These fits are similar to those performed for *ASCA* observations of the hard state of Cyg X-1 (Ebisawa et al. 1996), which shows evidence for a weak and narrow Fe line with equivalent width $\approx$40 eV, as well as for a soft excess well modeled as a multicolor blackbody with peak temperature $\approx$150 eV.

The fits with the phenomenological models yield $\chi^2_{\rm red}$ ranging from 0.98 to 1.4. The brightest data set showed the greatest evidence for structure beyond this simple model. A sample fit is shown in Figure 1. Note that the neutral hydrogen column was fixed to 6×10^{21} cm^{-2}. Allowed to freely vary, the neutral hydrogen column tended to float between 4 and 8×10^{21} cm^{-2}, depending upon what combination of phenomenological models was chosen, with minimal changes in the χ^2 of the fits. Associated with these changes in the best-fit neutral hydrogen column were $\gtrsim \pm 30\%$ changes of the best-fit peak temperature of the multicolor blackbody and even larger changes (factors of $\approx$3) in the best-fit normalization of the multicolor blackbody component. We should thus associate systematic error bars with these two parameters that are somewhat larger than the statistical error bars presented in Table 2.

All fits improved with the addition of a narrow Gaussian line. In all fits we fixed the line width to 0.1 keV (see Ebisawa et al. 1996; who always found $\sigma < 0.1$ keV in fits to *ASCA* data of Cyg X-1), and for the lowest flux data set we also fix the line energy to 6.4 keV. For the lowest flux data set, $\Delta\chi^2 = 5.5$ for one additional parameter. By the *F*-test (Bevington & Robinson 1992), this is an improvement to the fit for one additional parameter at the 98% confidence level. The other two data sets show even more significant

TABLE 2

PARAMETERS FOR A MULTICOLOR BLACKBODY PLUS BROKEN POWER-LAW PLUS GAUSSIAN LINE FITS TO *ASCA* DATA

Date	$T_{\rm in}$ (keV)	$A_{\rm dbb}$ ($\times 10^4$)	Γ_1	$E_{\rm b}$ (keV)	Γ_2	$A_{\rm bpl}$ ($\times 10^{-2}$)	$E_{\rm l}$ (keV)	$A_{\rm l}$ ($\times 10^{-4}$)	EW (eV)	χ^2/dof	$\chi^2_{\rm red}$
1994 Aug 24.....	$0.14^{+0.01}_{-0.02}$	$2.2^{+0.9}_{-1.6}$	$1.78^{+0.03}_{-0.03}$	$3.4^{+0.4}_{-0.5}$	$1.62^{+0.04}_{-0.03}$	$4.2^{+0.1}_{-0.1}$	...	...	...	1500/1439	1.04
1994 Aug 24.....	$0.14^{+0.01}_{-0.02}$	$2.2^{+0.7}_{-1.6}$	$1.78^{+0.03}_{-0.03}$	$3.3^{+0.5}_{-0.6}$	$1.64^{+0.03}_{-0.03}$	$4.2^{+0.1}_{-0.1}$	*6.4*	$0.6^{+0.4}_{-0.3}$	34^{+25}_{-19}	1494/1438	1.04
1994 Sep 12	$0.15^{+0.01}_{-0.01}$	$2.5^{+0.6}_{-1.0}$	$1.81^{+0.02}_{-0.01}$	$3.8^{+0.2}_{-0.2}$	$1.56^{+0.03}_{-0.03}$	$7.2^{+0.1}_{-0.1}$	...	...	...	1603/1621	0.99
1994 Sep 12	$0.15^{+0.00}_{-0.00}$	$2.5^{+0.1}_{-0.4}$	$1.81^{+0.01}_{-0.01}$	$3.8^{+0.1}_{-0.1}$	$1.59^{+0.01}_{-0.02}$	$7.2^{+0.0}_{-0.1}$	$6.36^{+0.08}_{-0.09}$	$1.6^{+0.7}_{-0.2}$	56^{+26}_{-7}	1580/1619	0.98
1995 Sep 08	$0.19^{+0.00}_{-0.01}$	$2.4^{+0.1}_{-0.3}$	$1.93^{+0.02}_{-0.01}$	$3.7^{+0.1}_{-0.1}$	$1.60^{+0.01}_{-0.02}$	$25.6^{+0.3}_{-0.3}$	...	...	...	2597/1838	1.41
1995 Sep 08	$0.19^{+0.00}_{-0.00}$	$2.4^{+0.0}_{-0.1}$	$1.93^{+0.01}_{-0.00}$	$3.7^{+0.1}_{-0.0}$	$1.63^{+0.01}_{-0.01}$	$25.6^{+0.0}_{-0.1}$	$6.51^{+0.07}_{-0.06}$	$3.3^{+0.6}_{-0.5}$	40^{+7}_{-6}	2523/1836	1.37

NOTES.—$T_{\rm in}$: Peak multicolor blackbody temperature. $A_{\rm dbb}$: Multicolor blackbody normalization. Γ_1, Γ_2: Broken power-law photon indexes. $E_{\rm b}$: Break energy. $A_{\rm bpl}$: Power-law normalization (photons keV^{-1} cm^{-2} s^{-1} at 1 keV). $E_{\rm l}$: Line energy. $A_{\rm l}$: Line normalization (photons cm^{-2} s^{-1} in the line). EW: Line equivalent width. Uncertainties are at the 90% confidence level for one interesting parameter ($\Delta\chi^2 = 2.71$). Parameters set in italic type have been held constant for that particular fit.

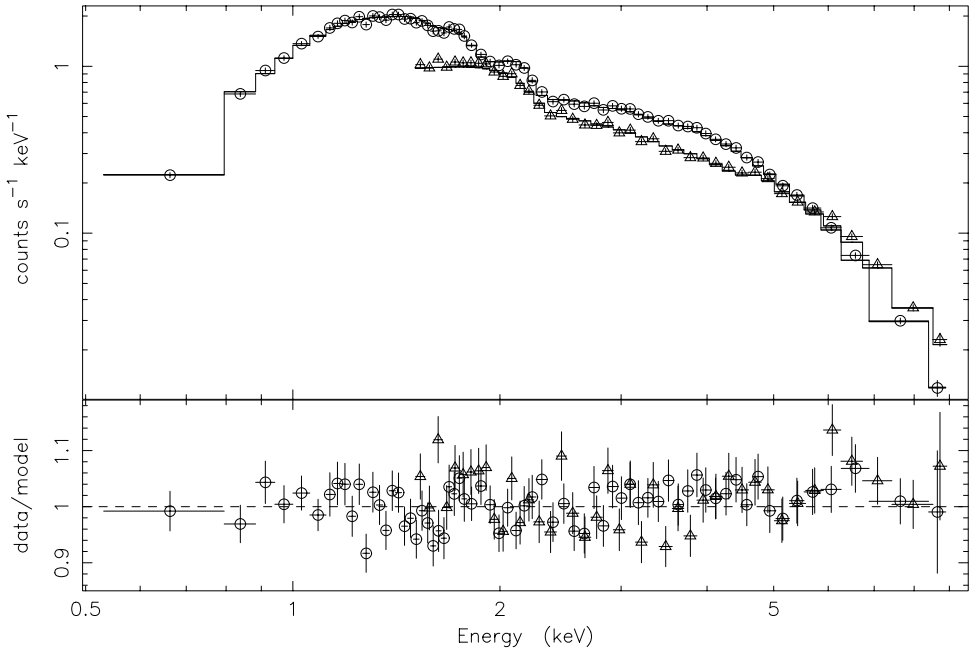

FIG. 1.—GX 339−4 *ASCA* observation of 1994 August 24, with energy bins rebinned by a factor of 25 for clarity. Model and associated residuals (data/model) are for the best-fit multicolor blackbody plus broken power law without a Gaussian line component. For clarity, only the SIS0 (*circles*) and GIS2 (*triangles*) data are shown.

improvements to χ^2. The best-fit line equivalent widths ranged from ≈ 30 to 60 eV. There is no compelling evidence for a strong flux dependence to the equivalent width of the line.

The transition to the bright, soft state typically occurs at 3–9 keV luminosities $\gtrsim 10^{-9}$ ergs cm^{-2} s^{-1}; i.e., factors of 2–10 brighter than these *ASCA* observations. Thus these observations offer useful tests of ADAF models, which are hypothesized to be most relevant to low-luminosity, hard-state systems (Narayan 1996; Esin, McClintock, & Narayan 1997). ADAF models predict a detectable correlation between the temperature of the soft excess, the strength of the Fe line, and the source luminosity. They hypothesize that the luminosity decay of BH transients is due, in part, to an increase of the radius at which the accretion flow transits from cold, geometrically thin, and radiatively efficient to hot, geometrically thick, and advective (Esin et al. 1997). In some models, the transition radius can grow to as large as $\mathcal{O}(10^4 R_G)$, where $R_G \equiv GM/c^2$. (Such large transition radii are not a strict requirement of ADAF models; in § 3.2.4 we show that somewhat smaller transition radii, ≈ 200–$400 R_G$, are preferred for ADAF models of the *RXTE* data.) As discussed by Esin et al. (1997), one then expects the peak temperature of the soft excess to decrease below 150 eV and the equivalent width of any Fe line to decrease to values less than ≈ 30 eV.

The best-fit equivalent widths found for GX 339−4 are greater than can be accommodated in ADAF models with a large transition radius, and they are also slightly larger than predicted by the "sphere + disk" corona models described in § 3.2.3 (see also Dove et al. 1997b, 1998). These latter models have a similar geometry to the ADAF models, and they often posit a coronal radius $\lesssim 100 R_G$. Likewise, we do not detect any large decreases in the best-fit disk temperatures with decreasing luminosity. Although it is dangerous to make a one-to-one correspondence between a phenomenological fit component and a physical component, these best-fit values are suggestive of, but not definitive proof of, temperatures hotter than can be accommodated in models in which cold, soft X-ray–emitting material exists at very large radii.

3. *RXTE* OBSERVATIONS

3.1. *The Monitoring Campaign*

To study the long-term behavior of GX 339−4, and to place our pointed observations within the context of the overall behavior of the source, we used data from the All Sky Monitor (ASM) on *RXTE*. The ASM provides light curves in three energy bands, 1.3–3.0 keV, 3.0–5.0 keV, and 5.0–12.2 keV, typically consisting of several 90 s measurements per day (see Levine et al. 1996; Remillard & Levine 1997; Lochner & Remillard 1997). In Figure 2 we present the ASM data of GX 339−4 until Truncated Julian Date (TJD) ≈ 1000 (1998 July 6). We also indicate the dates of our *RXTE* observations, as well as the dates of ATCA and MOST radio observations (Fender et al. 1997; Corbel et al. 1997; Hannikainnen et al. 1999). We discuss the long-timescale variability of this light curve in Paper II.

Based on model fits to the observations of Grebenev et al. (1991) (low and high state) and Miyamoto et al. (1991) (very high state), we expect the different states of GX 339−4 to have ASM count rates as indicated in Table 3. The *ASCA* and *RXTE* observations discussed here are most characteristic of weak to average luminosity hard states. Confirmation that the eight *RXTE* observations taken between TJD 481 and 749 do indeed represent a typical low/hard state comes from the broadband spectral analysis presented in § 3, as well as from the timing analysis presented in Paper II. The X-ray variability of these observations show root mean square variability of $\mathcal{O}(30\%)$ and show a power spectrum (PSD) that, roughly, is flat below 0.1 Hz, $\propto f^{-1}$ between

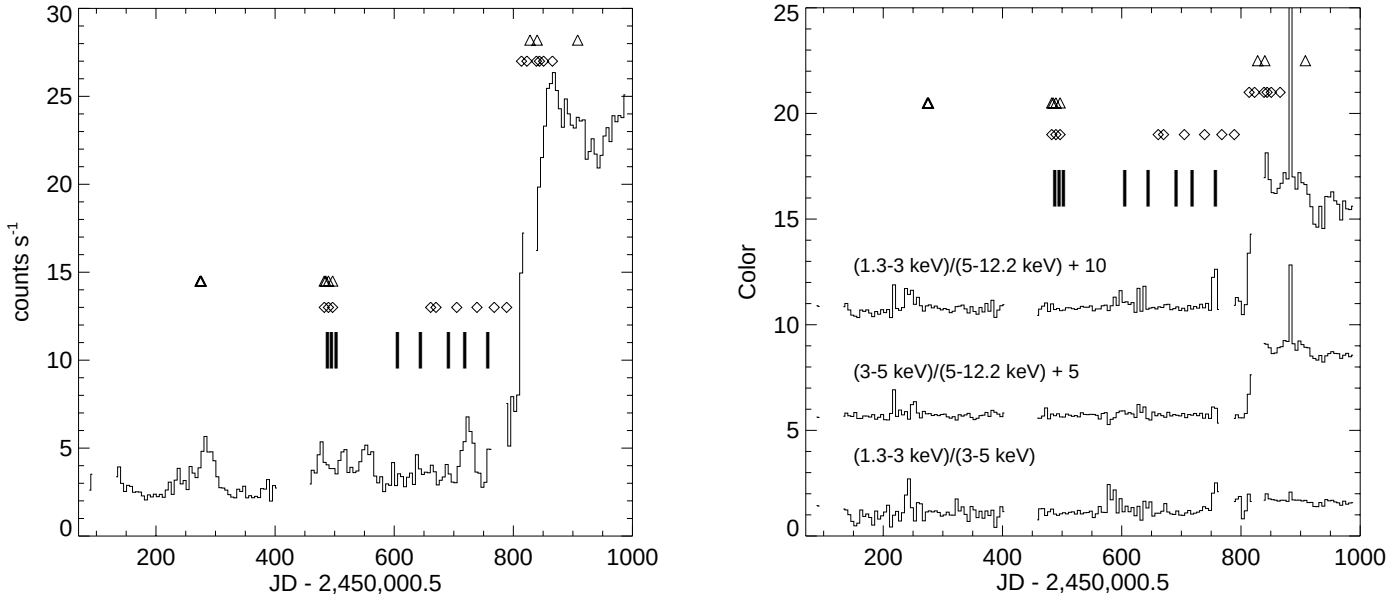

FIG. 2.—*Left panel: RXTE* All Sky Monitor data for GX 339−4 (5 day averages in the 1.3–12.2 keV band) vs. Truncated Julian Date (TJD) ≡ Julian Date (JD) −2450000.5. Vertical bars indicate dates of our *RXTE* pointed observations, diamonds indicate dates of MOST radio observations (Hannikainnen et al. 1999), and triangles indicate dates of ATCA radio observations (Fender et al. 1997; Corbel et al. 1997). *Right panel:* ASM colors for GX 339−4 vs. TJD. Colors shown are (1.3–3 keV)/(3–5 keV), (3–5 keV)/(5–12 keV) + 5, and (1.3–3 keV)/(5–12.2 keV) + 10 (the latter two colors have been offset for clarity).

0.1–3 Hz, and $\propto f^{-2}$ above 3 Hz. Time lags and coherence functions were also comparable to previously observed hard states of Cygnus X-1 (see Paper II, and references therein). Further discussion and analyses of the timing data can be found in Paper II.

The transition to a higher flux level that occurs at TJD ≈ 800 appears to have a characteristic flux of a high state but is not as soft in the 2–10 keV bands as expected from the above cited high and very high states. This might be an example of what Méndez & van der Klis (1997) refer to as an "intermediate state" between hard and soft. No pointed *RXTE* observations were taken during the transition, and four pointed observations, which were not part of our monitoring campaign, occurred shortly after the transition. Detailed confirmation of the spectral state suggested by the ASM data awaits analysis of these pointed observations. Note that the radio flux became quenched over the course of this transition to a higher ASM flux level (Fender et al. 1999).

The variations observed in both the ASM light curve (prior to TJD ≈ 800) and the pointed *RXTE* observations discussed below represent more than a factor 5 variation in observed flux. Comparable variations have been observed in the radio, and furthermore the radio light curves show evidence of a correlation with both the ASM and Burst and Transient Survey Explorer (BATSE) light curves (Hannikainnen et al. 1999).

TABLE 3

APPROXIMATE EXPECTED ASM COLORS FOR THE DIFFERENT STATES OF GX 339−4

	Count Rate (counts s^{-1})	1.3–3 keV / 3–5 keV	1.3–3 keV / 5–12.2 keV
Low.....	7	2	2
High	15	4	30
Very high.....	60	4	15

3.2. *PCA and HEXTE Observations*

In this section we present the results from our analysis of the data from the two pointed instruments on *RXTE*: the Proportional Counter Array (PCA), and the High-Energy X-Ray Timing Experiment (HEXTE). See Appendix B for a description of the instruments and of the details of the data extraction and processing. A log of the *RXTE* pointed observations and the simultaneous radio observations is given in Table 4.

As we show in Appendix B, there is a difference in the power-law slopes obtained from an analysis of spectra of the Crab with both instruments on *RXTE*. In order to minimize the impact of this difference in the instrumental calibration onto the data analysis, we primarily analyze the data from both instruments individually and use the difference in model parameters between instruments as a gauge of the systematic uncertainties. We do perform some joint analysis of PCA and HEXTE data using various reflection models. In the following sections we discuss in detail the implications of the calibration uncertainty for our analysis.

For our analysis of the *RXTE* broadband spectrum, we used several different spectral models consistent with the range of parameterizations currently used in the literature to describe the spectra of BHCs. As in the *ASCA* analysis (§ 2), we fixed $N_{\rm H} = 6 \times 10^{21}$ cm^2. We first used the purely phenomenological exponentially cut-off power-law and broken power-law models as a broad characterization of the data. The results of this modeling are given in § 3.2.1 and in Tables 5 and 6. We then applied the three more physically motivated models that are currently discussed in the literature: reflection of a power law off an (ionized) accretion disk (§ 3.2.2 and Table 7), "sphere and disk" corona Comptonization models (§ 3.2.3 and Table 8), and ADAF

TABLE 4

LOG OF *RXTE* AND RADIO OBSERVATIONS

OBSERVATION	DATE	TJD	T (ks)	RATE (counts s^{-1})	FLUX (10^{-9} ergs cm^{-2} s^{-1}) 3–9 keV	9–30 keV	30–100 keV	ATCA (mJy)	MOST (mJy)	α
01	1997 Feb 02	481	11	830	1.07	1.68	2.65	9.1 ± 0.2	7.0 ± 0.7	0.11
02	1997 Feb 10	489	10	730	0.94	1.50	2.41	8.2 ± 0.2	6.3 ± 0.7	0.11
03	1997 Feb 17	496	8	700	0.90	1.43	2.35	8.7 ± 0.2	6.1 ± 0.7	0.15
04	1997 Apr 29	567	10	470	0.60	0.97	1.55			
05	1997 Jul 07	636	10	200	0.25	0.43	0.75			
06	1997 Aug 23	683	11	650	0.74	1.18	1.98			
07	1997 Sep 19	710	10	730	0.96	1.48	2.36			
08	1997 Oct 28	749	10	480	0.63	1.01	1.68			

NOTES.—We list T, the duration of the *RXTE* observations; the average PCA count rate; the average (3–9 keV), (9–30 keV), and (30–100 keV) energy fluxes (all normalized to the PCA calibration); the flux density of the 8.3–9.1 GHz ATCA observations; the flux density of the 843 MHz MOST observations; and $\alpha = \Delta \log \nu / \Delta \log S_\nu$, the spectral index of the radio observations (Fender et al. 1997; Corbel et al. 1997; Hannikainnen et al. 1999).

models (§ 3.2.4). The ADAF models are applied to only the unfolded data. Residuals for each of the best fits to the data from observations 5 and 7 are shown in Figures 3, 4, and 5 (except for the ADAF models, for which we present observations 1 and 5). We chose to present these former two observations not only because are they at extremes in terms of observed luminosity (observation 5 is the faintest, and observation 7 is the second brightest; Table 4), but also because they show detectable differences in their timing properties (Paper II).

3.2.1. *Phenomenological Models*

Results from the purely phenomenological fits to the data, i.e., the broken power law and exponentially cut-off power law, are presented in Tables 5 and 6. We see that a broken power law plus a Gaussian line models the PCA data very well. The low $\chi^2_{\rm red}$ (0.15–0.32) indicates that to some extent we may be fitting systematic features in the PCA response. The same may be true for the best-fit parameters of the Fe line. The line widths ($\sigma \approx 0.6$ keV) and equivalent widths ($\approx$130 eV) are larger than for the *ASCA* observations, with the exception of observation 5, which has line parameters comparable to the *ASCA* observations. As observation 5 has the lowest count rate, it is more dominated by statistical errors and less dominated by systematic errors than the other observations. Even ignoring the possible systematic effects, however, we see that any observed line is narrower and weaker than is commonly observed in active galactic nuclei.

The $\approx$3–10 keV spectral power-law slope is close to the canonical value of $\Gamma = 1.7$; however, the PCA shows evidence for a hardening of this spectral slope above $\approx$10 keV.

TABLE 5

PARAMETERS FOR GAUSSIAN LINE PLUS BROKEN POWER-LAW MODELS AND GAUSSIAN LINE PLUS CUT-OFF BROKEN POWER-LAW MODELS

Observation	$E_{\rm line}$ (keV)	σ (keV)	$A_{\rm line}$ ($\times 10^{-3}$)	EW (eV)	Γ_1	$E_{\rm break}$ (keV)	Γ_2	$A_{\rm bkn}$	χ^2/dof	$\chi^2_{\rm red}$
01	$6.48^{+0.14}_{-0.15}$	$0.6^{+0.2}_{-0.2}$	$1.97^{+0.42}_{-0.36}$	130^{+24}_{-22}	$1.80^{+0.01}_{-0.01}$	$11.2^{+0.3}_{-0.4}$	$1.53^{+0.02}_{-0.02}$	$0.44^{+0.01}_{-0.01}$	13.6/ 52	0.26
02	$6.47^{+0.15}_{-0.16}$	$0.6^{+0.2}_{-0.2}$	$1.73^{+0.40}_{-0.35}$	129^{+26}_{-24}	$1.80^{+0.01}_{-0.01}$	$10.9^{+0.4}_{-0.4}$	$1.53^{+0.02}_{-0.02}$	$0.38^{+0.01}_{-0.01}$	16.6/52	0.32
03	$6.47^{+0.14}_{-0.15}$	$0.5^{+0.2}_{-0.2}$	$1.55^{+0.29}_{-0.31}$	121^{+24}_{-23}	$1.79^{+0.01}_{-0.01}$	$10.9^{+0.4}_{-0.4}$	$1.53^{+0.02}_{-0.03}$	$0.37^{+0.01}_{-0.01}$	13.5/ 52	0.26
04	$6.45^{+0.08}_{-0.15}$	$0.5^{+0.2}_{-0.2}$	$1.05^{+0.25}_{-0.22}$	121^{+28}_{-23}	$1.78^{+0.01}_{-0.01}$	$10.8^{+0.4}_{-0.5}$	$1.54^{+0.03}_{-0.03}$	$0.24^{+0.00}_{-0.00}$	20.7/ 52	0.38
05	$6.43^{+0.15}_{-0.17}$	$0.2^{+0.3}_{-0.2}$	$0.31^{+0.09}_{-0.08}$	84^{+25}_{-21}	$1.72^{+0.01}_{-0.01}$	$10.8^{+0.8}_{-0.8}$	$1.49^{+0.04}_{-0.05}$	$0.09^{+0.00}_{-0.00}$	22.9/ 52	0.44
06	$6.40^{+0.14}_{-0.15}$	$0.5^{+0.2}_{-0.2}$	$1.32^{+0.28}_{-0.27}$	123^{+23}_{-23}	$1.80^{+0.01}_{-0.01}$	$10.9^{+0.4}_{-0.4}$	$1.51^{+0.03}_{-0.03}$	$0.30^{+0.01}_{-0.01}$	25.2/ 52	0.48
07	$6.45^{+0.13}_{-0.13}$	$0.6^{+0.2}_{-0.2}$	$1.92^{+0.38}_{-0.34}$	140^{+23}_{-23}	$1.83^{+0.01}_{-0.01}$	$10.9^{+0.3}_{-0.4}$	$1.55^{+0.02}_{-0.02}$	$0.42^{+0.01}_{-0.01}$	27.3/ 52	0.53
08	$6.40^{+0.14}_{-0.15}$	$0.5^{+0.2}_{-0.2}$	$1.20^{+0.27}_{-0.23}$	130^{+26}_{-23}	$1.79^{+0.01}_{-0.01}$	$10.8^{+0.5}_{-0.5}$	$1.54^{+0.03}_{-0.03}$	$0.26^{+0.01}_{-0.01}$	28.3/ 52	0.54

NOTES.—Gaussian line plus broken power-law models: PCA only, 52 dof. Parameters are described in the text.

TABLE 6

PARAMETERS FOR EXPONENTIALLY CUT-OFF POWER-LAW MODELS

Observation	Constant	Γ	$E_{\rm cut}$ (keV)	$A_{\rm PL}$	Constant	χ^2/dof	$\chi^2_{\rm red}$
01	*1.00*	$1.25^{+0.06}_{-0.06}$	101^{+18}_{-14}	$0.082^{+0.014}_{-0.012}$	$0.99^{+0.01}_{-0.01}$	69.2/ 80	0.87
02	*1.00*	$1.12^{+0.08}_{-0.08}$	79^{+13}_{-10}	$0.052^{+0.011}_{-0.009}$	$0.92^{+0.02}_{-0.02}$	69.0/ 80	0.86
03	*1.00*	$1.16^{+0.17}_{-0.18}$	94^{+63}_{-28}	$0.052^{+0.029}_{-0.019}$	$1.08^{+0.04}_{-0.04}$	71.8/ 80	0.90
04	*1.00*	$1.15^{+0.11}_{-0.11}$	85^{+25}_{-16}	$0.035^{+0.011}_{-0.009}$	$0.98^{+0.02}_{-0.02}$	76.2/ 80	0.95
05	*1.00*	$1.18^{+0.19}_{-0.23}$	115^{+85}_{-46}	$0.016^{+0.011}_{-0.007}$	$0.99^{+0.05}_{-0.05}$	71.3/ 80	0.89
06	*1.00*	$1.19^{+0.09}_{-0.09}$	103^{+29}_{-19}	$0.049^{+0.012}_{-0.010}$	$0.93^{+0.02}_{-0.02}$	87.9/ 80	1.10
07	*1.00*	$1.21^{+0.07}_{-0.08}$	95^{+20}_{-14}	$0.066^{+0.014}_{-0.012}$	$0.96^{+0.02}_{-0.02}$	101.5/ 80	1.27
08	*1.00*	$1.08^{+0.10}_{-0.10}$	81^{+19}_{-13}	$0.031^{+0.009}_{-0.007}$	$0.98^{+0.02}_{-0.02}$	106.6/ 80	1.33

NOTES.—HEXTE only, 80 dof. Parameters are described in the text. Parameters set in italic type have been held constant for that particular fit.

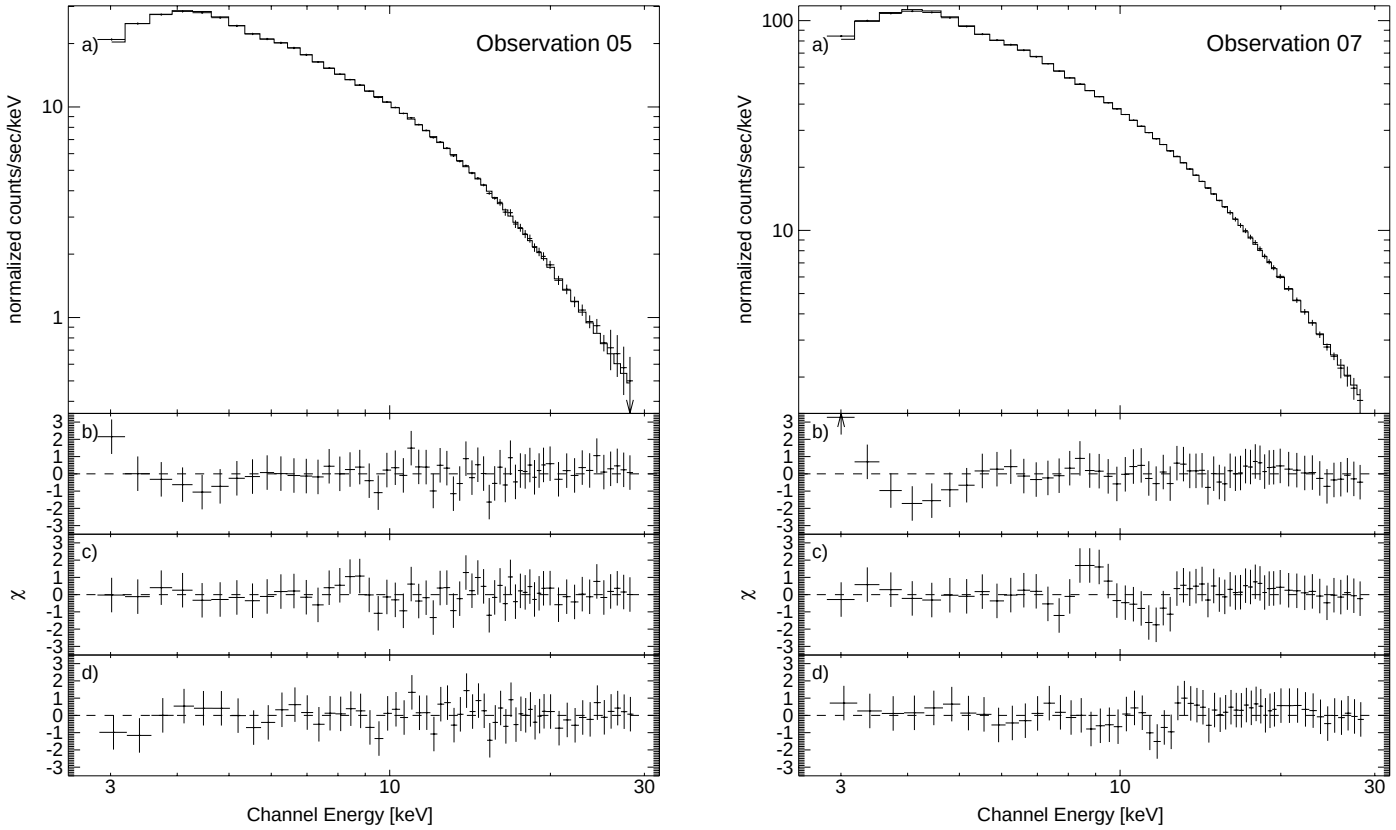

FIG. 3.—Spectral modeling of the PCA data from (*left panel*) observation 5 and (*right panel*) observation 7. Residues are shown as the contribution to χ. *In each panel:* (*a*) Count rate spectrum and the best-fit broken power law with a Gaussian line, (*b*) contribution to χ from the broken power law with a Gaussian line, (*c*) contribution to χ from the ionized reflection model (PEXRIV) with Gaussian line, and (*d*) contribution to χ from the sphere + disk model with an additional Gaussian line.

HEXTE data alone also show the high-energy spectrum to be harder than the 3–10 keV spectrum (Fig. 4 and Table 6). Note that the difference between the PCA and HEXTE photon indices is greater than the discrepancy between the PCA and HEXTE best-fit Crab photon indices (Appendix B), and therefore it is unlikely to be a systematic effect.

Such a hard HEXTE spectrum is consistent with previous observations by the Oriented Scintillation Spectrometer Experiment (OSSE) on board the *Compton Gamma-Ray Observatory* (*CGRO*) (Grabelski et al. 1995; see also Zdziarski et al. 1998). Grabelsky et al. (1995) found a slightly harder photon index of $\Gamma = 0.88$ and an exponential cutoff of $E_{\rm cut} = 68$ keV, somewhat lower than observed here. Note, however, that the OSSE observations extended to $\approx$500 keV as opposed to the $\sim$110 keV of our HEXTE observation. Therefore, the HEXTE data for GX 339−4 do not strongly constrain the exponential rollover, and slightly harder power laws with lower exponential cutoffs are permitted.

3.2.2. *Reflection Models*

A spectral hardening above $\approx$7 keV is the expected signature of reflection of a hard continuum off of cold material (Magdziarz & Zdziarski 1995). Ueda, Ebisawa, & Done (1994) applied reflection models to *Ginga* data of GX 339−4 and found strong evidence of reflection, whereas Grabelsky et al. (1995) found no evidence of reflection in OSSE data. Zdziarski et al. (1998) jointly fit these simultaneously observed data sets and find that reflection models, albeit with a large Fe abundance, provide a very good description of the data. We have applied the models of Magdziarz & Zdziarski (1995), as implemented in XSPEC (PEXRAV, PEXRIV), to the GX 339−4 data. These models consider an exponentially cut-off power law reflected off of neutral (PEXRAV) or partially ionized (PEXRIV) cold material.

In Table 7 we show the fit results for reflection off of partially ionized material similar to the models presented by Zdziarski et al. (1998). Just as in Zdziarski et al. (1998), we include a disk component where we fix the inner disk temperature to 250 eV. As PCA does not usefully constrain models below 3 keV, the disk component is not strongly constrained; typically the χ^2 values were higher by 5–20 without this component. We also fix the reflector inclination angle at 45°, fix the disk temperature at $T_{\rm disk} = 10^6$ K, and freeze the abundances at solar, but we let the Fe abundance be a free parameter. In all our fits we found that the Gaussian line width, σ, would tend to drift toward 0, so we fixed $\sigma = 0.1$ keV. For the combined PCA and HEXTE data, we also fixed the Gaussian line energy to 6.4 keV. For fits to PCA data alone and joint PCA/HEXTE data, the exponential cut-off energy, $E_{\rm fold}$, would drift toward very large energy ($\gg$1000 keV). We therefore considered only pure power laws without cutoffs. Zdziarski et al. (1998) have argued that the high-energy cutoff is sharper than exponential, which one would not expect to be strongly constrained by the combined PCA/HEXTE data.

As for the *Ginga* data of GX 339−4 (Ueda et al. 1994), the PCA data alone were extremely well described by reflection models. Again, however, the extremely low $\chi^2_{\rm red}$ (as low as

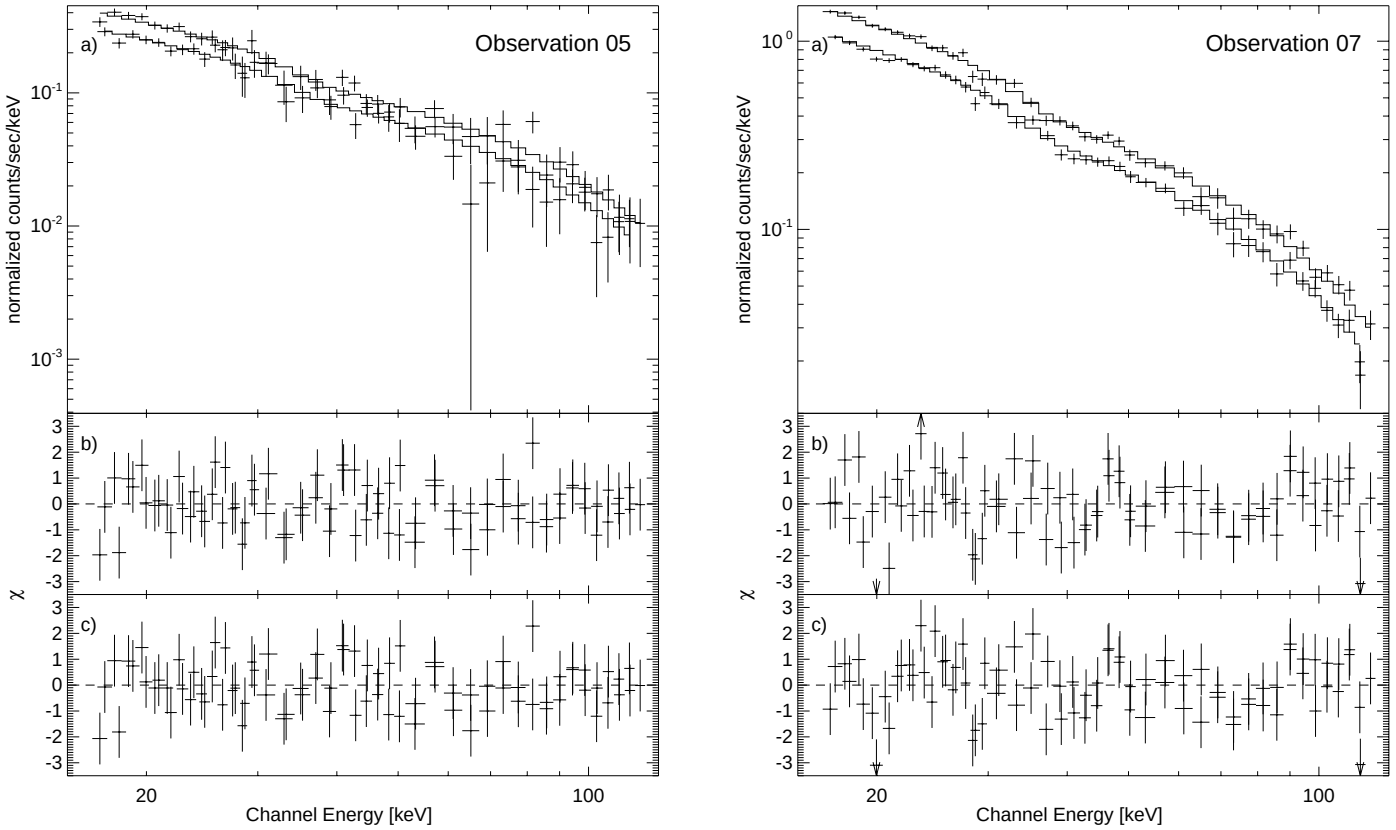

FIG. 4.—Spectral modeling of the HEXTE data from (*left panel*) observation 5 and (*right panel*) observation 7. Residues are shown as the contribution to χ. *In each panel:* (*a*) count rate spectrum and the best-fit power law with exponential cutoff, (*b*) contribution to χ from the power law with exponential cutoff, and (*c*) contribution to χ from the sphere + disk model.

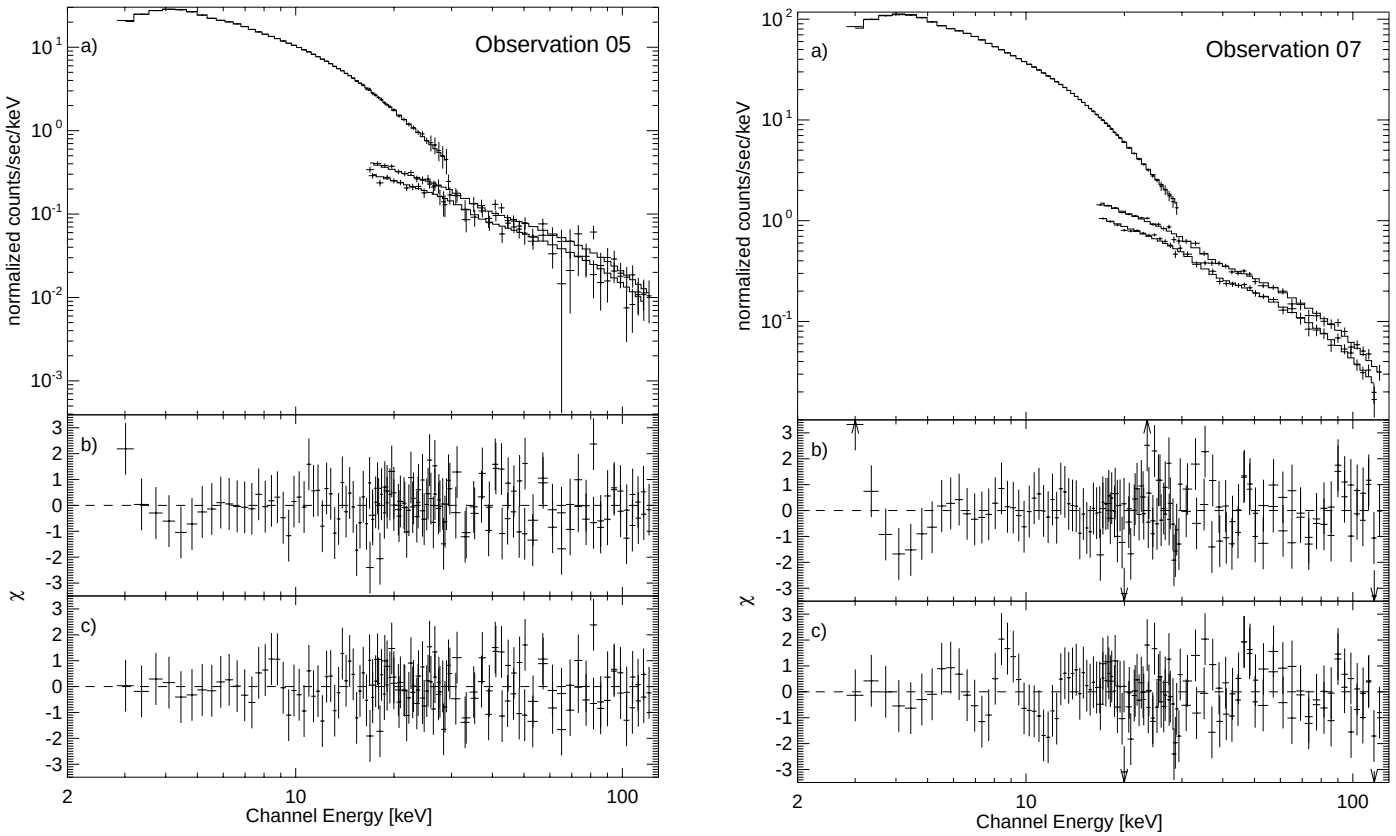

FIG. 5.—Spectral modeling of the joint PCA and HEXTE data for observation 5 and 7. Residues are shown as the contribution to χ. *In each panel:* (*a*) Count rate spectrum and the best-fit broken power law with a Gaussian line, (*b*) contribution to χ from the best-fit broken power law with a Gaussian line (parameters not given in text), and (*c*) contribution to χ from the best-fit ionized reflector model with a Gaussian line.

TABLE 7

PARAMETERS FOR GAUSSIAN LINE PLUS MULTICOLOR DISK PLUS IONIZED REFLECTION MODELS

Observation	$A_{\rm dbb}$	Γ ($\times 10^5$)	$\Gamma_{\rm HEXTE}$	f	$A_{\rm Fe}$ ($A_{\rm Fe_\odot}$)	ξ (ergs cm s^{-1})	$A_{\rm pex}$	$E_{\rm line}$ (keV)	$A_{\rm line}$ ($\times 10^{-4}$)	EW (eV)	Constant	Constant	χ^2/dof	$\chi^2_{\rm red}$
01	$1.64^{0.82}_{-0.83}$	$1.81^{+0.02}_{-0.02}$	...	$0.41^{+0.06}_{-0.05}$	$1.54^{+0.67}_{-0.40}$	$78.2^{+28.7}_{-23.7}$	$0.43^{+0.01}_{-0.01}$	$6.22^{+0.22}_{-0.23}$	$7.00^{+2.95}_{-3.10}$	41^{+18}_{-18}	...	...	25./51	0.49
01	$1.54^{+0.81}_{-0.82}$	$1.81^{+0.02}_{-0.02}$	$1.76^{+0.04}_{-0.03}$	$0.47^{+0.07}_{-0.06}$	$2.26^{+1.01}_{-0.65}$	$60.5^{+20.8}_{-21.8}$	$5.85^{+2.75}_{-2.98}$	*6.4*	$5.85^{+2.75}_{-2.98}$	35^{+18}_{-17}	$0.57^{+0.09}_{-0.07}$	$0.57^{+0.09}_{-0.07}$	113./132	0.86
02	$1.68^{+0.73}_{-0.73}$	$1.81^{+0.02}_{-0.02}$	...	$0.41^{+0.06}_{-0.05}$	$1.36^{+0.58}_{-0.36}$	$82.2^{+31.6}_{-23.9}$	$0.37^{+0.01}_{-0.01}$	$6.16^{+0.23}_{-0.25}$	$5.96^{+2.60}_{-2.82}$	40^{+17}_{-19}	...	...	21./51	0.41
02	$1.49^{+0.73}_{-0.73}$	$1.80^{+0.02}_{-0.02}$	$1.75^{+0.05}_{-0.04}$	$0.52^{+0.09}_{-0.07}$	$2.46^{+1.50}_{-0.80}$	$54.0^{+21.3}_{-22.5}$	$4.08^{+2.45}_{-2.68}$	*6.4*	$4.08^{+2.45}_{-2.68}$	18^{+28}_{-10}	$0.57^{+0.12}_{-0.08}$	$0.52^{+0.11}_{-0.07}$	124./132	0.94
03	$1.34^{+0.70}_{-0.69}$	$1.81^{+0.02}_{-0.02}$	...	$0.42^{+0.06}_{-0.05}$	$1.49^{+0.62}_{-0.42}$	$59.8^{+24.1}_{-24.8}$	$0.36^{+0.01}_{-0.01}$	$6.22^{+0.24}_{-0.27}$	$5.56^{+2.53}_{-2.66}$	39^{+16}_{-18}	...	...	14./51	0.28
03	$1.23^{+0.70}_{-0.70}$	$1.81^{+0.02}_{-0.02}$	$1.68^{+0.05}_{-0.05}$	$0.44^{+0.07}_{-0.06}$	$1.61^{+0.76}_{-0.46}$	$50.9^{+22.6}_{-22.9}$	$4.96^{+2.46}_{-2.56}$	*6.4*	$4.96^{+2.46}_{-2.56}$	36^{+19}_{-18}	$0.42^{+0.09}_{-0.07}$	$0.45^{+0.09}_{-0.07}$	89./132	0.68
04	$1.13^{+0.47}_{-0.48}$	$1.79^{+0.02}_{-0.02}$	...	$0.37^{+0.07}_{-0.06}$	$1.33^{+0.77}_{-0.43}$	$70.2^{+31.3}_{-27.3}$	$0.23^{+0.00}_{-0.01}$	$6.17^{+0.23}_{-0.23}$	$4.56^{+1.80}_{-1.90}$	47^{+18}_{-19}	...	...	15./51	0.30
04	$1.03^{+0.47}_{-0.47}$	$1.79^{+0.02}_{-0.02}$	$1.73^{+0.07}_{-0.05}$	$0.46^{+0.12}_{-0.08}$	$2.26^{+1.78}_{-0.86}$	$44.2^{+24.1}_{-23.7}$	$3.61^{+1.60}_{-1.88}$	*6.4*	$3.61^{+1.60}_{-1.88}$	39^{+18}_{-20}	$0.54^{+0.14}_{-0.09}$	$0.52^{+0.14}_{-0.08}$	100./132	0.76
05	$0.39^{+0.23}_{-0.24}$	$1.73^{+0.03}_{-0.02}$	...	$0.43^{+0.49}_{-0.13}$	$2.43^{+11.04}_{-1.35}$	$10.1^{+35.8}_{-10.1}$	$0.09^{+0.00}_{-0.00}$	$6.32^{+0.27}_{-0.27}$	$1.84^{+1.06}_{-0.94}$	48^{+29}_{-25}	...	...	18./51	0.34
05	$0.36^{+0.22}_{-0.23}$	$1.73^{+0.03}_{-0.02}$	$1.65^{+0.12}_{-0.08}$	$0.44^{+0.24}_{-0.12}$	$2.41^{+3.49}_{-1.22}$	$6.1^{+25.2}_{-6.1}$	$1.87^{+1.09}_{-0.96}$	*6.4*	$1.87^{+1.09}_{-0.96}$	50^{+30}_{-48}	$0.49^{+0.24}_{-0.12}$	$0.49^{+0.23}_{-0.12}$	88./132	0.67
06	$1.61^{+0.57}_{-0.57}$	$1.80^{+0.02}_{-0.02}$	...	$0.47^{+0.10}_{-0.07}$	$1.87^{+1.05}_{-0.56}$	$55.0^{+24.0}_{-24.2}$	$0.29^{+0.00}_{-0.01}$	$6.08^{+0.22}_{-0.23}$	$5.45^{+2.16}_{-2.30}$	45^{+18}_{-19}	...	...	17./51	0.33
06	$1.46^{+0.55}_{-0.55}$	$1.81^{+0.02}_{-0.02}$	$1.71^{+0.05}_{-0.04}$	$0.52^{+0.10}_{-0.07}$	$2.38^{+1.26}_{-0.74}$	$36.7^{+22.0}_{-19.2}$	$4.06^{+2.08}_{-2.05}$	*6.4*	$4.06^{+2.08}_{-2.05}$	26^{+30}_{-8}	$0.50^{+0.10}_{-0.07}$	$0.47^{+0.09}_{-0.07}$	113./132	0.86
07	$2.29^{+0.73}_{-0.73}$	$1.83^{+0.02}_{-0.02}$	...	$0.42^{+0.06}_{-0.05}$	$1.37^{+0.58}_{-0.37}$	$84.8^{+32.5}_{-23.9}$	$0.40^{+0.01}_{-0.01}$	$6.16^{+0.18}_{-0.19}$	$8.36^{+2.67}_{-2.96}$	54^{+18}_{-19}	...	...	25./51	0.48
07	$2.10^{+0.72}_{-0.72}$	$1.83^{+0.02}_{-0.02}$	$1.74^{+0.04}_{-0.03}$	$0.48^{+0.07}_{-0.06}$	$1.97^{+0.93}_{-0.57}$	$61.5^{+21.9}_{-22.7}$	$6.23^{+2.76}_{-2.48}$	*6.4*	$6.23^{+2.76}_{-2.48}$	43^{+20}_{-17}	$0.50^{+0.08}_{-0.06}$	$0.48^{+0.08}_{-0.06}$	144./132	1.09
08	$1.25^{+0.47}_{-0.47}$	$1.80^{+0.02}_{-0.02}$	...	$0.38^{+0.06}_{-0.05}$	$1.36^{+0.67}_{-0.42}$	$72.6^{+30.7}_{-26.6}$	$0.25^{+0.01}_{-0.01}$	$6.15^{+0.19}_{-0.20}$	$5.55^{+1.95}_{-1.87}$	55^{+19}_{-18}	...	...	18./51	0.35
08	$1.14^{+0.47}_{-0.47}$	$1.80^{+0.02}_{-0.02}$	$1.71^{+0.07}_{-0.05}$	$0.50^{+0.15}_{-0.09}$	$2.81^{+2.23}_{-1.11}$	$39.0^{+24.8}_{-21.7}$	$4.14^{+1.89}_{-1.72}$	*6.4*	$4.14^{+1.89}_{-1.72}$	44^{+20}_{-19}	$0.51^{+0.14}_{-0.09}$	$0.50^{+0.14}_{-0.09}$	141./132	1.07

NOTES.—After Magdziarz & Zdziarski 1995. Models have been fit to PCA data only (51 dof), and PCA and HEXTE data where the photon index of the reflected power law has been allowed to differ between the PCA and the HEXTE data (132 dof). Fit parameters are the normalization of the multicolor disk blackbody, $A_{\rm dbb}$ (the disk temperature has been fixed to 250 eV); the power-law slope, Γ; the cut-off energy, $E_{\rm fold}$; the relative reflection fraction, $f \equiv \Delta\Omega/2\pi$; the Fe abundance relative to solar, $A_{\rm Fe}$; the disk ionization parameter, $\xi \equiv$ luminosity/(density $\times$ radius^2); and a normalization, $A_{\rm pex}$. The ionized reflection models also have parameters for the temperature of the disk, $T_{\rm disk}$ (fixed at 10^6 K); abundances of elements heavier than He relative to solar, A_X (fixed at unity); and disk inclination angle, i (fixed at 45°). Parameters set in italic type have been held constant for that particular fit. The iron line width was fixed at 0.1 keV.

0.28) makes us caution that these models might partly be fitting systematics in the PCA response. PCA and *Ginga* are also very similar instruments in terms of design, and so to some extent they should exhibit similar systematic effects (as discussed in Appendix B, the internal consistency of the PCA calibration is now as good as or better than that of the *Ginga* calibration.). Note that the best-fit Fe line equivalent widths here are significantly smaller than those found with the purely phenomenological models discussed in § 3.2.1.

The fits for the HEXTE data alone (not shown) were similar to the OSSE results of Grabelsky et al. (1995). Namely, if one allows for an exponential cutoff (typically ≈ 100 keV) to the power law, the best-fit reflection fraction becomes $f \lesssim 0.01$. Such a small reflection fraction is not surprising considering how well a pure exponentially cut-off power law fits the HEXTE data (Table 6). If one does not allow an exponential cutoff, the reflection fraction becomes $f \gtrsim 3$. Such a fit is trying to mimic a hard power law with a high-energy cutoff.

A joint analysis of the PCA and the HEXTE data should be similar to a joint analysis of the Ginga and OSSE data. Indeed, such an analysis yields results comparable to those presented by Zdziarski et al. (1998) if we constrain the photon index of the incident power law to be the same for both the PCA and HEXTE data. Notable for the results of such fits (not presented) is the fairly large overabundance of Fe ($A_{\rm Fe} = 3.2$–5.2). Similarly, Zdziarski et al. (1998) find a large $A_{\rm Fe} = 2.5$–3.0 except for a short data set, more likely dominated by statistical errors rather than systematic errors, for which they find $A_{\rm Fe} = 1.6$–2.0. For our joint PCA/HEXTE data, the best-fit reflection fractions were approximately 20% larger than the best-fit reflection fraction for PCA data alone. Such an increase in reflection fraction in general will reproduce the spectral hardening seen in the HEXTE energy bands. Increasing the average best-fit Fe abundance from $\langle A_{\rm Fe}\rangle = 1.6$ (PCA data alone) to $\langle A_{\rm Fe}\rangle = 4.0$ (joint PCA/HEXTE data) also leads to an increased spectral hardening above ≈ 7 keV while leaving the spectrum below ≈ 7 keV relatively unchanged. That is, such a fit helps to reproduce the spectral break at ≈ 10 keV.

For the joint PCA/HEXTE analysis, there is clearly a worry that these results are influenced by the systematic differences between the PCA and the HEXTE responses. We therefore performed reflection model fits where we constrained all fit parameters to be the same for the PCA and the HEXTE data except for the incident power-law photon index, which we allowed to vary between the two instruments.[7] Such models provided reasonably good fits to the data, with $\chi^2_{\rm red}$ ranging from 0.67 to 1.09. The differences between the PCA and the HEXTE best-fit photon indices ranged from 0.05 to 0.13, with an average value of 0.08. This is consistent with the systematic difference between the best-fit photon indexes for the Crab spectrum. For these models we find $\langle A_{\rm Fe}\rangle = 2.3$, which is more consistent with the results for fits to the PCA data only and is slightly smaller than the results found by Zdziarski et al. (1998). Note that we also find smaller values of the ionization parameter, ξ, than were found by Zdziarski et al. (1998).

[7] The photon index was constrained to be the same for HEXTE Cluster A and B. The necessary different normalizations between the PCA and the HEXTE models were subsumed into the constants multiplying the HEXTE models. As HEXTE requires a harder power law, these constants were now 0.42–0.57, as opposed to ≈ 0.7. Furthermore, the constants showed larger uncertainties, as the uncertainty of the HEXTE photon index now couples strongly to the value of the constants.

3.2.3. *Corona Models*

We considered sphere + disk Comptonization models (Dove et al. 1997b) of the GX 339−4 observations. We have previously applied these models to an *RXTE* observation of Cygnus X-1 (Dove et al. 1998). The models each consist of a central, spherical corona surrounded by a geometrically thin, flat disk. Seed photons for Comptonization come from the disk, which has a radial temperature distribution $kT_{\rm disk}(R) \propto R^{-3/4}$ and a temperature of 150 eV at the inner edge of the disk. Hard flux from the corona further leads to reflection features from the disk or to soft photons due to thermalization of the hard radiation. The (nonuniform) temperature and pair balance within the corona are self-consistently calculated from the radiation field (Dove, Wilms, & Begelman 1997a; Dove et al. 1997b).

As described by Dove et al. (1997a, 1997b), we parameterize our models by the coronal compactness

$$\ell_c \equiv \frac{\sigma_{\rm T}}{m_e c^3}\frac{L_C}{R_C}, \tag{1}$$

where $\sigma_{\rm T}$ is the Thomson cross section, m_e is the electron mass, L_C is the luminosity of the corona, and R_C is the radius of the corona. Likewise, we define a disk compactness, $\ell_d \equiv (1 - f_c)(\sigma_{\rm T}/m_e c^3)P_G/R_C$, where P_G is the total rate of gravitational energy dissipated in the system, and f_c is the fraction dissipated in the corona. In calculating the numerical models, we set $\ell_d = 1$. Models with other values of ℓ_d yield the same ranges of self-consistent coronal temperatures and opacities. In general $f_c = \ell_c/(\ell_d + \ell_c)$ (Dove et al. 1997a). Based upon the sphere + disk geometry, a fraction $f \approx 0.32$ of the coronal flux is absorbed by the disk (Dove et al. 1997b). The models are further parameterized by an initial electron coronal optical depth, τ_c (approximately equal to the total optical depth, as pair production is negligible for the parameters of interest to us), and a normalization constant $A_{\rm kot}$. From the best-fit compactness and optical depth, the average coronal temperature can be calculated a posteriori.

Attempts to fit these models to the joint PCA/HEXTE data failed. Typical $\chi^2_{\rm red}$ values, even allowing for the inclusion of an extra Gaussian line component, were $\gtrsim 1.3$. These fits showed a clear tendency for a hardening in the HEXTE band, and therefore we considered them to be influenced by the cross-calibration uncertainties between the PCA and the HEXTE instruments (Note that our previous fits of Cyg X-1 used an earlier version of the PCA response in which we applied 1.5% systematic uncertainties across the entire PCA band; these fits yielded $\chi^2_{\rm red} \approx 1.6$, without considering an additional Gaussian component). We therefore considered sphere + disk models fit to the PCA and the HEXTE data separately. In Table 8, we present the best-fit parameters for these models applied to our GX 339−4 data.

Although our numerical sphere + disk models do include reflection and a fluorescent Fe line (typical equivalent width ≈ 25 eV) from the disk, the PCA data showed residuals in the 5–7 keV band, as in our fits to *RXTE* data of Cyg X-1 (Dove et al. 1998). We included an additional Gaussian component to our fits. The equivalent widths of the additional lines were ≈ 150 eV, and they appeared to be broad ($\sigma \approx 0.8$ keV). This additional line may be attributable partly to uncertainties in the PCA response. For these fits,

TABLE 8

MODELS OF "SPHERE + DISK" COMPTONIZATION PLUS GAUSSIAN LINE FITS TO PCA DATA ONLY AND TO HEXTE DATA ONLY

Observation	$E_{\rm Line}$ (keV)	σ (keV)	$A_{\rm Line}$ ($\times 10^{-3}$)	EW (eV)	l_c	τ_c	$A_{\rm kot}$	Constant	kT_c (keV)	χ^2/dof	$\chi^2_{\rm red}$
01	$6.39^{0.18}_{-0.17}$	$0.8^{+0.2}_{-0.1}$	$3.09^{+0.60}_{-0.53}$	197^{+30}_{-30}	$0.62^{+0.05}_{-0.04}$	$3.2^{+0.1}_{-0.1}$	$2.38^{+0.06}_{-0.08}$	...	$28.6^{+0.4}_{-0.4}$	19.2/53	0.36
01	...	...	...	...	$1.83^{+0.17}_{-0.13}$	$2.9^{+0.5}_{-0.3}$	$0.91^{+0.09}_{-0.09}$	$0.99^{+0.01}_{-0.01}$	43.9^{+8}_{-8}	71.2/80	0.89
02	$6.36^{+0.19}_{-0.19}$	$0.8^{+0.2}_{-0.1}$	$2.69^{+0.57}_{-0.50}$	194^{+41}_{-36}	$0.63^{+0.06}_{-0.05}$	$3.3^{+0.1}_{-0.1}$	$2.07^{+0.06}_{-0.07}$	...	$27.9^{+0.4}_{-0.4}$	15.7/53	0.30
02	...	...	...	...	$1.96^{+0.12}_{-0.12}$	$3.6^{+0.3}_{-0.3}$	$0.73^{+0.04}_{-0.03}$	$0.92^{+0.02}_{-0.02}$	34.0^{+3}_{-2}	67.6/80	0.84
03	$6.36^{+0.21}_{-0.16}$	$0.8^{+0.2}_{-0.2}$	$2.42^{+0.44}_{-0.49}$	182^{+33}_{-37}	$0.66^{+0.06}_{-0.06}$	$3.4^{+0.1}_{-0.1}$	$1.95^{+0.06}_{-0.06}$	...	$27.9^{+0.4}_{-0.4}$	16.7/53	0.31
03	...	...	...	...	$2.21^{+0.48}_{-0.34}$	$3.4^{+0.7}_{-1.1}$	$0.61^{+0.17}_{-0.08}$	$1.08^{+0.04}_{-0.04}$	37.4^{+26}_{-7}	72.4/80	0.90
04	$6.40^{+0.22}_{-0.17}$	$0.8^{+0.2}_{-0.2}$	$1.53^{+0.32}_{-0.34}$	174^{+36}_{-39}	$0.70^{+0.08}_{-0.07}$	$3.6^{+0.1}_{-0.1}$	$1.27^{+0.05}_{-0.05}$	...	$26.6^{+0.4}_{-0.4}$	13.5/53	0.25
04	...	...	...	...	$2.09^{+0.19}_{-0.22}$	$3.4^{+0.6}_{-0.5}$	$0.46^{+0.04}_{-0.04}$	$0.98^{+0.02}_{-0.02}$	36.9^{+9}_{-6}	78.1/80	0.98
05	$6.28^{+0.31}_{-0.97}$	$0.9^{+0.3}_{-0.3}$	$0.52^{+0.73}_{-0.17}$	138^{+100}_{-100}	$0.68^{+0.15}_{-0.08}$	$4.4^{+0.3}_{-0.1}$	$0.53^{+0.02}_{-0.02}$	...	$20.6^{+0.4}_{-0.4}$	20.5/53	0.39
05	...	...	...	...	$2.89^{+0.78}_{-0.65}$	$3.1^{+1.1}_{-2.0}$	$0.16^{+0.03}_{-0.03}$	$0.99^{+0.05}_{-0.05}$	44.9^{+103}_{-13}	71.8/80	0.90
06	$6.26^{+0.24}_{-0.22}$	$0.9^{+0.2}_{-0.2}$	$2.06^{+0.50}_{-0.46}$	186^{+45}_{-42}	$0.66^{+0.07}_{-0.05}$	$3.6^{+0.1}_{-0.1}$	$1.57^{+0.04}_{-0.06}$	...	$26.2^{+0.4}_{-0.4}$	16.5/53	0.31
06	...	...	...	...	$2.33^{+0.21}_{-0.18}$	$3.1^{+0.6}_{-0.4}$	$0.54^{+0.08}_{-0.04}$	$0.93^{+0.02}_{-0.02}$	42.3^{+11}_{-8}	88.7/80	1.11
07	$6.40^{+0.19}_{-0.18}$	$0.8^{+0.2}_{-0.2}$	$2.67^{+0.56}_{-0.49}$	192^{+41}_{-35}	$0.65^{+0.06}_{-0.05}$	$3.3^{+0.1}_{-0.1}$	$2.06^{+0.05}_{-0.07}$	...	$28.4^{+0.4}_{-0.4}$	15.6/53	0.30
07	...	...	...	...	$1.99^{+0.13}_{-0.16}$	$3.1^{+0.4}_{-0.4}$	$0.75^{+0.09}_{-0.04}$	$0.96^{+0.02}_{-0.02}$	40.7^{+10}_{-6}	102.9/80	1.29
08	$6.34^{+0.23}_{-0.21}$	$0.9^{+0.2}_{-0.2}$	$1.74^{+0.40}_{-0.40}$	189^{+43}_{-43}	$0.71^{+0.08}_{-0.07}$	$3.7^{+0.1}_{-0.1}$	$1.30^{+0.05}_{-0.05}$	...	$25.9^{+0.4}_{-0.4}$	15.5/53	0.29
08	...	...	...	...	$2.37^{+0.29}_{-0.23}$	$3.7^{+0.4}_{-0.5}$	$0.43^{+0.03}_{-0.03}$	$0.98^{+0.02}_{-0.02}$	34.6^{+7}_{-5}	109.0/80	1.36

NOTES.—The three fit parameters of the Comptonization model are the compactness of the corona, ℓ_c, the coronal optical depth, τ_c, and a normalization constant, $A_{\rm kot}$. The Gaussian line is parameterized as in the previous tables. From the best-fit parameters, the equivalent width of the line, EW, and the density averaged coronal temperature, kT_c, are derived.

as well as for the reflection model fits, lines with energies significantly less than 6.4 keV can be fit, and this is likely a systematic effect. Part of the discrepancy between the data and the model, however, is significant. As we have discussed for our fits to the *RXTE* Cyg X-1 data, there are several possible physical interpretations for the additional required equivalent width: there may be an overlap between the disk and the sphere (our models invoke a sharp transition), the disk may be flared (we model a flat disk), the disk may have nonsolar abundances, or, alternatively, one might invoke a "patchy disk" embedded in the corona (Zdziarski et al. 1998). The best-fit reflection fractions of $f \approx 0.4$–0.5 found above are further indication that our models may require an additional source of reflected flux.

Allowing an additional Gaussian line component, the fits to the PCA data yield extremely low $\chi^2_{\rm red}$, which could be indicating that we are partly fitting systematic features in the PCA response. Note also that the PCA data fits yielded consistently larger optical depths and consistently lower compactness parameters than the HEXTE data fits. The latter was more significant and is again indicative of the HEXTE response being harder than the PCA response. Both instruments yielded optical depths $\tau_c \approx 3$–4; however, because of the discrepancy in the best-fit spectral slopes between the PCA and the HEXTE bands, the best-fit average coronal temperatures range from 21–30 keV (PCA) to 34–45 keV (HEXTE).

3.2.4. *ADAF Models*

The basic picture of mass accretion via an ADAF in the context of Galactic BHCs was introduced by Ichimaru (1977) and has been elaborated upon in a series of papers by Narayan and collaborators (Narayan, Kato, & Honma 1997; Esin et al. 1997). The accretion flow is divided into two distinct zones: the inner part is modeled as a hot, optically thin ADAF similar in some respects to the spherical corona discussed above, while the outer part consists of a standard optically thick, geometrically thin disk. The transition radius between the two zones, $r_{\rm tr} = R_{\rm tr}/R_G$, is one of the model parameters. We compute the ADAF spectrum according to the procedure described by Di Matteo et al. (1999). The electrons in an ADAF cool via three processes: bremsstrahlung, synchrotron radiation, and inverse Compton scattering. In addition we add the emission from a thin disk—calculated as a standard multicolor blackbody—and include the Compton reflection component due to the scattering of high-energy photons incident on the disk.

In the ADAF models discussed here, we fix the black hole mass to be $m \equiv M/M_\odot = 6$, assume the magnetic field to be in equipartition with thermal pressure ($\beta = 0.5$), and set the standard Shakura-Sunyaev viscosity parameter (Shakura & Sunyaev 1973) to be $\alpha_{\rm SS} = 0.3$. We normalize the accretion rate to $\dot{m} \equiv \dot{M}c^2/L_{\rm Edd}$, where $L_{\rm Edd}$ is the Eddington luminosity of the source. The hard state corresponds to mass accretion rates $\dot{m} \leq \dot{m}_{\rm crit} = 10^{-2}$, where $\dot{m}_{\rm crit}$ is the critical value above which an ADAF no longer exists. As $\dot{m}$ increases toward $\dot{m}_{\rm crit}$, the scattering optical depth of the ADAF goes up which causes the spectrum to become harder and smoother. Most of the flux from the ADAF plus disk configuration is emitted around 100 keV, and the spectrum falls off at higher energies.

The model spectrum changes mainly as a function of $r_{\rm tr}$ and $\dot{m}$. The various spectral states correspond to different values of these parameters. For example, Esin et al. (1997) attempt to explain the initial transition from soft to hard seen in the decay of Nova Muscae by a large change in $r_{\rm tr}$ (from $r_{\rm tr} \approx 10$ to $r_{\rm tr} \approx 10^4$), followed by an exponential decay in $\dot{m}$ for the subsequent evolution of this transient system. The *ASCA* data of GX 339−4 discussed in § 2 imply that comparably large changes in $r_{\rm tr}$ are not relevant to those observations. Here, however, unfolded *RXTE* data from observations 1 and 5, the brightest and faintest observations, respectively, can be described by ADAF models with $r_{\rm tr} = 200$, $\dot{m} = 0.08$ and $r_{\rm tr} = 400$, $\dot{m} = 0.05$, respectively. These model spectra and *RXTE* spectra for observations 1 and 5 unfolded with a cut-off broken power law plus a Gaussian line are shown in Figure 6. In these ADAF models, the observed spectral and luminosity changes of GX 339−4 are predominantly driven by changes in the

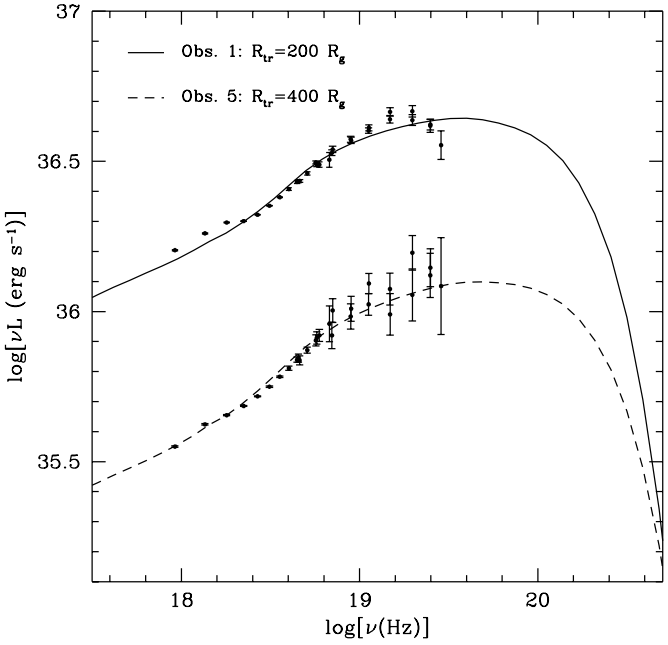

FIG. 6.—Advection-dominated accretion flow models for the unfolded *RXTE* data from observation 1 (*solid line*) and observation 5 (*dot-dashed line*). Parameters consistent with the unfolded data are described in the text. A source distance of 4 kpc was assumed.

transition radius; the implied accretion rate change is substantially smaller than the factor of 5 for the observed luminosity change.

For $r_{\rm tr} \sim 200$, which provides a rough description of observation 1, the disk blackbody emission peaks in the far UV/soft X-rays and dominates over the synchrotron emission, which peaks in the optical/UV (see also Zdziarski et al. 1998). The peak synchrotron emission frequency scales as $\propto m^{-1/2}\dot{m}^{1/2}r_{\rm tr}^{5/4}$ and peaks in the range $\nu = 10^{11}$–10^{12} Hz for supermassive black holes and $\nu = 10^{15}$–10^{16} Hz for Galactic black holes. The spectrum below the peak is approximately $S_\nu \propto \nu^2$. The synchrotron emission can contribute significantly to the radio emission of supermassive black holes (although see Di Matteo et al. 1999); however, the predicted radio flux of GX 339−4 is ten orders of magnitude below the observed 7 mJy flux at 843 MHz. Thus, there must be an extended source of radio emission, which we further discuss in the next section.

4. SIMULTANEOUS RADIO OBSERVATIONS

The first three of our *RXTE* observations were simultaneous with 843 MHz observations taken with the Molongolo Observatory Synthesis Telescope (MOST) and with 8.3–9.1 GHz observations taken at the Australian Telescope Compact Array (ATCA). Extensive discussion of the MOST and ATCA observations can be found in Hannikainnen et al. (1999) and Corbel et al. (1997), respectively (see also Table 4).

An estimate of the minimum size of the radio emitting region can be obtained by noting that,observationally, the brightness temperatures of radio sources usually are not larger than 10^{12} K; otherwise, the electrons will suffer catastrophic inverse Compton losses. The brightness temperature of a uniformly bright spherical source is given by $(cD/d\nu)^2 S_\nu/2\pi k$, where d is the diameter of the source, D is its distance, ν is the observed radio frequency, S_ν is the observed radio flux density, c is the speed of light, and k is the Boltzmann constant. Taking the 7 mJy observed at 843 MHz by MOST and the fact that GX 339−4 is unresolved, we derive

$$d \gtrsim 4 \times 10^{12}\ {\rm cm}\left(\frac{D}{4\ {\rm kpc}}\right) \approx 3 \times 10^6 R_G \left(\frac{D}{4\ {\rm kpc}}\right)\left(\frac{M}{10\ M_\odot}\right)^{-1}, \quad (2)$$

which is orders of magnitude larger than the inferred size of the X-ray–emitting region, even for models that posit extremely extended coronae (e.g., Esin et al. 1997; Kazanas, Hua, & Titarchuk 1997).

This size scale is $\propto \nu^{-1}$, so emission at 8.6 GHz could arise in a region an order of magnitude smaller than that responsible for the emission at 843 MHz. Indeed, the flat spectrum emission is likely to arise in a conical jet with a radially decreasing optical depth (e.g., Hjellming & Johnston 1988). Thus the outflow likely has an extent of $\mathcal{O}(10^7 GM/c^2)$ or greater. Similar estimates for source size have been made for the other persistent black hole candidate and Z-source neutron star X-ray binaries by Fender & Hendry (1999).

Assuming a radio spectral index of $\alpha = 0.1$ and a sharp cutoff at 10 μm (a reasonable upper limit for where the synchrotron flux becomes optically thin, and typical of where ADAF models become optically thin to synchrotron), the synchrotron flux is approximately 0.1% of the 3–100 keV X-ray flux. The correlation between the X-ray and radio fluxes found by Hannikainnen et al. (1999), comparable to the X-ray/radio correlation observed in Cyg X-1 (Pooley, Fender & Brocksopp 1999), suggests that there is a coupling between the inner accretion disk and the extended outflow on timescales of 7 days or less. Matter leaving the corona at the escape velocity ($0.25c$ at $30R_G$) and thereafter decelerating under the influence of gravity would take roughly 7 days to travel a distance of $10^7 R_G$. As 7 days is the upper bound to the correlation timescale, the radio-emitting outflow must leave at slightly greater than escape velocity, or there must be at least some amount of acceleration of the outflow.

Although the radio observations are strictly simultaneous with our first three *RXTE* observations, GX 339−4 exhibits less than 1% rms variability over the shortest timescales for which a reasonable radio flux estimate can be made ($\gtrsim$10 minutes). Thus there are no strong features to correlate between the radio and X-ray bands.

5. DISCUSSION

5.1. *Coronal Size and Luminosity Variation*

The relationship between the inferred size of the corona and the magnitude of the observed flux depends upon which spectral model we are considering. As discussed in § 3.2.4, for ADAF models one can associate lower fluxes with increased coronal radii. A larger coronal radius implies a lower efficiency and hence a decreased observed flux, even for constant accretion rates. Paper II shows that the characteristic power spectral density (PSD) timescale for GX 339−4 decreases for the lowest observed flux (observation 5). If one associates the PSD timescale with characteristic disk timescales, this could be in agreement with an increased coronal radius. However, in Paper II we also

show that the time lag between hard and soft X-ray variability decreases with decreasing flux, which seems counter to a positive correlation between flux and coronal size.

The sphere+disk coronal models make no assumptions about the radiative efficiency of the accretion. The flux can be either positively or negatively correlated with coronal radius, depending upon the variations of the coronal compactness, ℓ_c, and the temperature, T_d, at the inner edge of the accretion disk that surrounds the corona (Dove et al. 1997b). Note that the sphere+disk models used in this work, unlike those in many ADAF models, do not consider synchrotron photons as a source of seed photons for Comptonization.

Using the definitions of ℓ_c, ℓ_d, and f given in § 3.2.3, energy balance in the sphere+disk system determines the coronal radius, to within factors of order unity, to be given by

$$R_C \approx 160\left(\frac{\ell_d + f\ell_c}{\ell_d + \ell_c}\right)^{1/2}\left(\frac{kT_d}{150\ \mathrm{eV}}\right)^{-2}\left(\frac{6\ M_\odot}{M}\right) \times \left(\frac{D}{4\ \mathrm{kpc}}\right)\left(\frac{F_{\mathrm{tot}}}{10^{-8}\ \mathrm{ergs\ cm^{-2}\ s^{-1}}}\right)^{1/2} R_G\,, \quad (3)$$

where M is the mass of the compact object, D is the distance to the source, and F_{tot} is the bolometric flux of the source. If T_d, f, ℓ_d, and ℓ_c were held fixed, then the coronal radius would be positively correlated with flux. Whereas this might pose some problems for understanding the flux dependence of the characteristic timescales observed in the PSD, this would agree with the flux dependence of the X-ray variability time lags (Paper II). However, as the *RXTE* bandpass does not usefully extend below ≈ 3 keV, we do not have a good understanding of the flux dependence of T_d. If $T_d \propto F_{\mathrm{tot}}^{\beta}$ with $\beta > 1/4$, then increasing flux could imply decreasing coronal radius.

5.2. *Correlation among Spectral Parameters*

Ueda et al. (1994) claimed that reflection models of GX 339−4 exhibited a correlation between photon index, Γ, and reflection fraction, f, with softer spectra implying greater reflection. Zdziarski (1999) has claimed that this correlation extends to reflection models of Seyfert 1 galaxies as well. To expect such a correlation is not unreasonable. For example, if we allow the corona and disk to overlap to some extent in the sphere+disk model (Poutanen, Krolik, & Ryde 1997), then we expect the increase in the flux of seed photons to cool the corona and lead to a softer spectral index. Likewise, the covering fraction of the disk would be increased, in agreement with the suggested correlation. In Figure 7 we plot f versus Γ for our reflection model fits to GX 339−4. Contrary to the claims of Ueda et al. (1994) and Zdziarski (1999), however, there is no strong evidence for a correlation. Fitting the reflection fraction with a function linear in Γ, as opposed to fitting with the mean value of f, improves the χ^2 of the fits by 0.2, which is not significant. Fitting with the mean gives $\chi^2_{\mathrm{red}} = 0.2$.

We do note two possible trends from the reflection model fits. First, as has been noted for other hard-state Galactic black hole candidates (Tanaka & Lewin 1995; and references therein), there may be a correlation between flux and photon index, with lower flux implying a harder source. (The significance of the correlation is driven by observation 5, the faintest and hardest of the observations. However, a

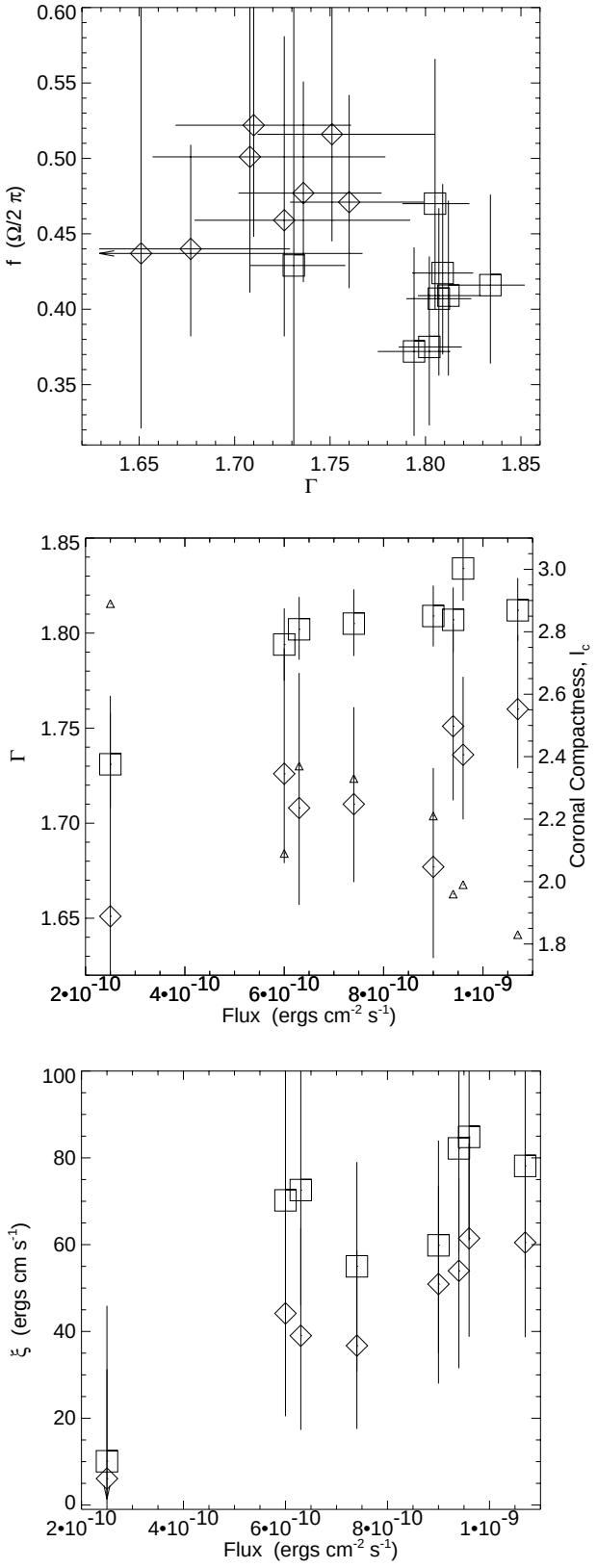

FIG. 7.—*Left panel:* Reflection fraction vs. photon index, Γ, for models fit to PCA data only (*squares*), and models fit to PCA plus HEXTE data that allowed the PCA and HEXTE photon indexes and normalizations to be different (*diamonds*; HEXTE photon index shown). *Middle panel:* Photon index, Γ, vs. observed 3–9 keV flux for the same reflection models as on the left. Also shown, without error bars, is the best-fit compactness, ℓ_c, for sphere+disk coronal models fit to HEXTE data (*small triangles*). *Right panel:* Disk ionization parameter, ξ, in units of ergs cm s^{-1} for the same reflection models as in the left panel.

similar correlation is also present in color-intensity diagrams.) Such a correlation is consistent with the expectations of ADAF models, in which the radius increases with decreasing flux (Fig. 6). Again, the sphere + disk corona models do not predict a clear trend without knowledge of the flux dependences of other parameters such as T_d.

Second, the ionization parameter, ξ, is positively correlated with flux. Such a correlation was noted by Życki, Done, & Smith (1998) for Ginga observations of Nova Muscae. It is not unreasonable to expect the disk to become increasingly ionized with increasing flux. We again caution that it is dangerous to make one-to-one correlations between a model fit parameter and a true physical parameter. Furthermore, the significance of the correlation is again almost entirely determined by observation 5, the faintest observation, which has $\xi \approx 0$. However, if we take the flux dependence of ξ as being real and interpret it physically, it provides some constraints on the flux dependence of the coronal radius. The ionization parameter is $\propto F_{\rm tot}/(\rho R^2)$, where ρ is the density of the disk. For a gas pressure–dominated Shakura-Sunyaev α disk, $\rho \propto R^{-1.65}$ (Shakura & Sunyaev 1973). In order for ξ to be roughly linear in flux (the actual dependence is not strongly constrained by the data), we require $F_{\rm tot} \propto R^{1.35}$. (For the sphere + disk models this would further require that approximately $T_d \propto R^{-1/3}$, depending upon the flux dependences of ℓ_d, ℓ_c, g, etc.) Taken physically and in the context of a gas pressure–dominated Shakura-Sunyaev α model, the flux dependence of ξ implies that the coronal radius increases with increasing flux.

6. SUMMARY

We have presented a series of observations of the black hole candidate GX 339−4 in low-luminosity, spectrally hard states. These observations consisted of three separate archival *ASCA* and eight separate *RXTE* data sets. All of these observations exhibited (3–9 keV) flux $\lesssim 10^{-9}$ ergs s^{-1} cm^{-2}, and the observed fluxes spanned roughly a factor of 5 in range for both the *ASCA* and *RXTE* data sets. Subject to uncertainties in the cross calibration between *ASCA* and *RXTE*, the faintest *ASCA* observation was approximately a factor of 2 fainter than the faintest *RXTE* observation.

All of these observations showed evidence for an $\approx$6.4 keV Fe line with equivalent widths in the range of $\approx$20–140 eV. The *ASCA* observations further showed evidence for a soft excess that was well modeled by a power law plus a multicolor blackbody spectrum with peak temperatures in the range $\approx$150–200 eV. Both of these factors considered together argue against sphere + disk or ADAF type–geometry coronae with extremely large coronal radii of $\mathcal{O}(10^4 R_G)$ (e.g., Esin et al. 1997).

The *RXTE* data sets were well fit by sphere + disk Comptonization models with coronal temperatures in the range 20–50 keV and optical depths near $\tau \approx 3$. These fits were similar to our previous fits to *RXTE* data of Cyg X-1. Advection-dominated accretion flow models, which posit a similar geometry, also provided reasonable descriptions of the unfolded *RXTE* data. The sphere + disk and ADAF models were not able, however, to also model the observed radio fluxes. Thus, a static corona seems to be ruled out by the observations. The ADAF models can imply that the coronal radius increases with decreasing flux. The sphere + disk corona models do not make a specific prediction for the dependence of the coronal radius on the flux; however, they can be consistent with a positive correlation between coronal radius and flux. As described in Paper II, a positive correlation between flux and coronal radius is consistent with the observed flux dependence of the time lags between hard and soft X-ray variability.

We also considered "reflection models" of the *RXTE* data. These models showed evidence of a hardening of the *RXTE* spectra with decreasing X-ray flux. They further showed evidence of a positive correlation between the best-fit ionization parameter, ξ, and the observed flux. Especially the latter of these correlations, however, was dominated by the model fits of the faintest observation. The reflection models did not exhibit any evidence of a correlation between the photon index of the incident power-law flux and the solid angle subtended by the reflector.

Three of the *RXTE* observations were strictly simultaneous with 843 MHz and 8.3–9.1 GHz radio observations. The most likely source of the radio flux is synchrotron emission from an extended outflow with a size of $\mathcal{O}(10^7 GM/c^2)$. The correlation between radio and X-ray emission on timescales of 7 days or less (Hannikainnen et al. 1999) implies a strong coupling of the inner disk accretion flow with this spatially extended outflow as is expected by recent theoretical arguments (Blandford & Begelman 1999). Further simultaneous radio/X-ray observations, preferably with the addition of IR/optical monitoring to constrain the location of the synchrotron break and with the addition of soft X-ray monitoring to constrain the accretion disk parameters, are required to test such models in detail.

We would like to thank Christopher Reynolds for keeping a stiff upper lip while explaining *ASCA* data analysis to us. We would also like to thank K. Mukai of the *ASCA* GOF for useful advice. W. A. Heindl and D. Gruber kindly provided assistance with the HEXTE data extraction, and S. Corbel provided assistance with the radio data. We are grateful to B. Stern for writing the original version of KOTELP, and, more importantly, for finally telling us what the name means ("cauldron"). We would also like to acknowledge useful conversations with B. Begelman, J. Chiang, B. A. Harmon, K. Pottschmidt, R. Staubert, C. Thompson, and A. Zdziarski. This work has been financed by NASA Grants NAG 5-4731 and NAG 5-3225 (M. A. N., J. B. D.). M. N. was supported in part by the National Science Foundation under Grant Phy94-07194. J. W. was supported by a travel grant from the Deutscher Akademischer Austauschdienst, R. P. F. was supported by an EC Marie Curie Fellowship (ERBFMBICT 972436), and T. D. M. thanks Trinity College and PPARC for financial support. This research has made use of data obtained through the High Energy Astrophysics Science Archive Research Center Online Service, provided by the NASA/Goddard Space Flight Center.

APPENDIX A

ASCA DATA EXTRACTION

We extracted data from the two solid state detectors (SIS0, SIS1) and the two gas detectors (GIS2, GIS3) on board *ASCA* by using the standard FTOOLS as described in the *ASCA* Data Reduction Guide (Day et al. 1998). The data extraction radius was limited by the fact that all the observations were in one-CCD mode and that the source was typically placed close to the chip edge. We chose circular extraction regions with radii of $\approx 4'$ for SIS0, $\approx 3'$ for SIS1 (the maximum possible extraction radii for these detectors), and $\approx 6'$ for GIS2 and GIS3. For observation 3 we excluded the central 40″ to avoid the possibility of photon pileup. We used the SISCLEAN and GISCLEAN tools (with default values) to remove hot and flickering pixels. We filtered the data with the strict cleaning criteria outlined in the *ASCA* Data Analysis Handbook; however, we took the larger value of 7 GeV/c for the rigidity. We rebinned the spectral files so that each energy bin contained a minimum of 20 photons. We retained SIS data in the 0.5–9 keV range and GIS data in the 1.5–9 keV range.

We accounted for the cross-calibration uncertainties of the three instruments by introducing a multiplicative constant for each detector in all of our fits. Relative to SIS0, the SIS1 detector normalization was always found to be within 2%, the GIS2 normalization was found to be within 9%, and the GIS3 normalization was found to be within 15%. For any given observation, the normalization constants varied by $\lesssim \pm 1\%$ for different spectral fits. The background was measured from rectangular regions on the two edges of the chip farthest from the source (SIS data), or from annuli with inner radii $>6'$ (GIS data). These data were cleaned and filtered in the same manner as the source files.

The resulting data files showed reasonable agreement between all four detectors. The most discrepant detector was SIS1, which also was the detector limited to the smallest extraction radius. This detector tended to show deviations from the other detectors for energies $\gtrsim 9$ keV, and from the SIS0 detector for energies ≈ 0.5–1 keV. The detectors were mostly in mutual agreement for the lowest flux observations. It is likely that the agreement could be further improved for observations located closer to the center of the chips (thereby allowing larger extraction radii) and if low–Galactic latitude dark sky observations in one-CCD mode were available to use as background.

APPENDIX B

RXTE DATA EXTRACTION

In § 3 we present data from both pointed instruments on *RXTE*, the Proportional Counter Array (PCA) and the High-Energy X-Ray Timing Experiment (HEXTE). As we showed in § 3, the large effective area of these instruments results in a data analysis approach that is dominated by the calibration uncertainty of these detectors (especially the PCA). In this appendix we summarize the major properties of both instruments and study their (inter-) calibration. All *RXTE* results obtained in this paper were obtained using the standard *RXTE* data analysis software, FTOOLS version 4.1 (including the *RXTE* patch 4.1.1 and the correct accounting of the time dependence of the PCA response; K. Jahoda 1998, private communication). Spectral modeling was done using XSPEC, version 10.00s (Arnaud 1996).

The PCA consists of five nearly identical coaligned Xenon proportional counter units (PCUs) with a total effective area of about 6500 cm^2. The instrument is sensitive in the energy range from 2 to ~ 60 keV (Jahoda et al. 1996). We used only data for which all five PCUs were turned on. Background subtraction was done in the same manner as for our *RXTE* Cyg X-1 observations (Dove et al. 1998). Specifically, a model using the rate of Very Large Events in the detector was used to estimate the background flux. The major uncertainty of this estimated background is due to activation of radioactivity in the detectors during South Atlantic Anomaly passages. Since this background component is present for about 30 minutes after the passage, we ignored data measured during these intervals. Furthermore, data were not accumulated at times of high electron contamination. The electron contamination is measured by a certain ratio of veto rates in the detectors, the so-called electron ratio (Jahoda et al. 1999). As recommended by the *RXTE* Guest Observer's Facility (GOF), we excluded times during which the "electron ratio" was larger than 0.1 in at least one of the detectors. Note that the observed count rates from GX 339−4 are too high to allow the use of the newer background model made available by the *RXTE* GOF in 1998 June.

For spectral fitting, we limited the energy range of the PCA data from 3 to 30 keV and used version 2.2.1 of the PCA response matrices. These matrices are newer than those used by us previously (Dove et al. 1998), and they are primarily characterized by assuming a higher instrumental resolution (Jahoda et al. 1999). Because of the large PCA count rate of GX 339−4 (~ 800 counts s^{-1}) our observations are dominated by the remaining uncertainties in the detector calibration and not by Poisson errors. Therefore, a good understanding of these uncertainties is necessary.

Since the Crab spectrum is commonly assumed to be a featureless power law (Toor & Seward 1974), at least over narrow energy ranges, the ratio between the fit to the Crab and the data can be used to deduce the systematic uncertainty associated with the detector calibration. We therefore extracted a public domain spectrum of the Crab nebula and pulsar measured with the PCA on 1997 April 1. The Crab data were screened using the same criteria as those applied to our GX 339−4 data, except for that the "electron ratio" check was not applied since the background contributes only 0.6% to the total number of photons detected for the Crab. Modeling the 3 to 30 keV Crab data with an absorbed power law resulted in a best-fit photon spectrum of the form

$$N_{\rm ph} = 13.3E^{-2.187} \exp\left[-2.54 \times 10^{21}\ {\rm cm}^{-2}\sigma_{\rm bf}(E)\right]\ {\rm cm}^{-2}\ {\rm s}^{-1}\ {\rm keV}^{-1}\ , \quad \text{(B1)}$$

where $\sigma_{\rm bf}(E)$ is the energy dependent bound-free absorption cross section for material of cosmic abundances as given by Morrison & McCammon (1983), and where E is the photon energy measured in keV. For this fit to the Crab data,

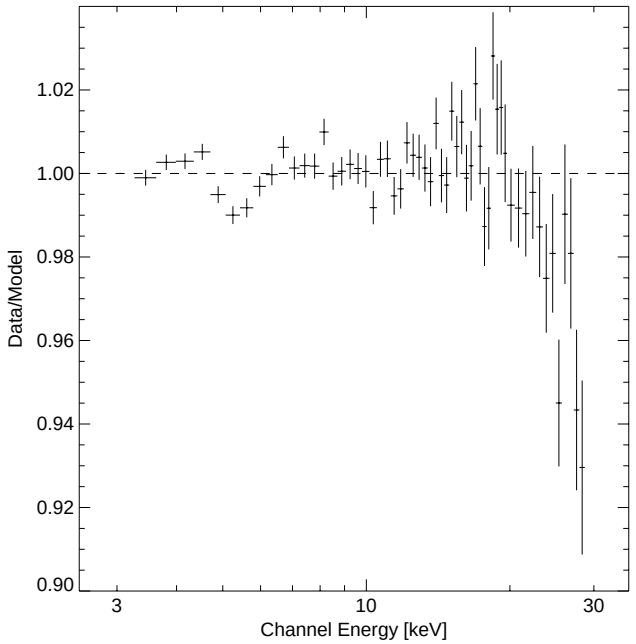

FIG. 8.—Ratio between the power-law fit of eq. (B1) and the PCA Crab nebula data. The major deviations between the data and the model are due to the Xe $L_{1,2,3}$ edges at ~ 5.1 keV and to the Xe K edge at 34.6 keV.

$\chi^2/\mathrm{dof} = 168/56$. In Figure 8 we display the ratio between the best fit to the Crab and the data. Using this ratio plot, we deduced the systematic uncertainties of the detector (Table 9). Adding them in quadrature to the Poisson errors of our data, the χ^2 of the above Crab fit was reduced to $\chi^2_{\mathrm{red}} = 0.56$. Note that the internal consistency of the detector calibration of the PCA appears to be on the 1% level, i.e., comparable to that obtained for previously flown instruments like the *Ginga* LAC (Turner et al. 1989) or the *ASCA* GIS (Makishima et al. 1996), even though the much larger effective area of the PCA makes it necessary to include many "dirt effects" into the detector model.

We caution that the statistical uncertainties of the fit parameters presented in this work were derived using the above systematic uncertainties. It is questionable, therefore, whether the approach of Lampton, Margon, & Bowyer (1976) to determine the uncertainties from the χ^2 contours can really be used since this approach makes use of the assumption of Poisson-type errors. The uncertainties given in this work should be taken with these caveats in mind, especially for those fits for which the χ^2_{red} values are very small (i.e., $\lesssim 0.5$), and thus they should not be construed literally as "90% uncertainties."

The HEXTE consists of two clusters of four Na I/Cs I–phoswich scintillation counters, sensitive from 15 to 250 keV. A full description of the instrument is given by Rothschild et al. (1998). Source-background rocking of the two clusters provides a direct measurement of the HEXTE background with measured long-term systematic uncertainties of $<1\%$ (Rothschild et al. 1998). Although no other strong sources in the field around GX $339-4$ are known (Covault, Grindlay, & Manandhar 1992; Bouchet et al. 1993; Trudolyubov et al. 1998), we extracted individual background spectra for both HEXTE cluster background positions to check for contamination of the spectrum from weak background sources. In all cases the background spectra differed by $\lesssim 1$ count s^{-1}. Thus, we used the added background spectra from both cluster positions in our data analysis. We used the standard response matrices dated 1997 March 20 and used data measured between 17 and 110 keV. An analysis of the detector calibration similar to that performed for the PCA reveals that the HEXTE calibration is good on a level comparable to the PCA. Because of the much smaller effective area of the detector and because of the smaller flux from the source at higher energies, however, the HEXTE spectrum is completely dominated by the Poisson error of the data. Therefore we did not attempt to take the systematic calibration uncertainty into account. To improve the statistics of individual energy bins, we rebinned the raw (≈ 1 keV wide) energy channels by a factor of 2 for the energy range from 30 to 51 keV, and by a factor of 3 above that.

TABLE 9

SYSTEMATIC UNCERTAINTIES OF VERSION 2.2.1 OF THE PCA RESPONSE MATRIX AS OBTAINED FROM A POWER-LAW FIT TO THE CRAB SPECTRUM (FIG. 8)

	CHANNEL[a]			
PARAMETER	0–15	16–39	40–57	58–128
Channel energy (keV).....	0–7	7–16	16–25	>25
Uncertainty (%)	1	0.5	2	5

[a] PCA channels assuming the standard2 channel binning.

When modeling the spectrum of GX 339−4 from 3 to 110 keV as measured by the PCA and the HEXTE, the intercalibration between the instruments is of some concern. Our experience with previous data and the response matrix described by Dove et al. (1998) indicated that the flux calibration of the HEXTE with respect to the PCA was off by about 25%; i.e., the derived HEXTE fluxes were ~75% of those found with the PCA. This deviation is mainly due to a slight misalignment of the HEXTE collimators, which has not yet been taken into account in the HEXTE response matrix (B. Heindl 1998, private communication). Using the new PCA response, the flux ratio now appears to be larger and was found to be 62%–69% in our data. Extracting spectra with internal software used by the HEXTE hardware team produced spectra identical to those found using our extraction procedure. Therefore we do not believe this change in the flux calibration to be due to errors in the dead-time correction. To take this offset in the effective areas into account, we modeled the spectra using a multiplicative constant that was set to unity for the PCA, and that was a fit parameter for both HEXTE clusters. Thus, all fluxes given below were measured with respect to the PCA. The maximum deviation of the HEXTE clusters relative to each other was found to be less than 8%.

Apart from the flux calibration, however, even more crucial for our analysis is the question of how well the inferred spectral shapes agree for the two instruments. Our Crab fits show that the PCA results in a photon index of $\Gamma = 2.187$ (eq. [B1]), while our HEXTE fits gave $\Gamma = 2.053$. The generally accepted value for the Crab photon index in the 1–100 keV range is $\Gamma = 2.10 \pm 0.03$. This value was adopted by Toor & Seward (1994) in their analysis of 28 different rocket flight measurements. There are indications that the spectrum softens to $\Gamma \sim 2.5$ above 150 keV (Jung 1989). Although the absolute uncertainty of the Crab flux in the 2–100 keV range has been estimated as large as 2%, and even larger below 2 keV (Nørgaard-Nielsen et al. 1994), the $\Delta\Gamma = 0.134$ deviation between the PCA and the HEXTE best-fit Crab photon index is still very worrisome, and it is currently being studied by both the PCA and HEXTE instrument teams (K. Jahoda 1998, private communication).

REFERENCES

Arnaud, K. A. 1996, in ASP Conf. Ser. 101, Astronomical Data Analysis Software and Systems V, ed. J. H. Jacoby & J. Barnes (San Francisco: ASP), 17
Bevington, P. R., & Robinson, D. K. 1992, Data Reduction and Error Analysis for the Physical Sciences (2d ed.; New York: McGraw-Hill)
Blandford, R. D., & Begelman, M. C. 1999, MNRAS, 303, 1
Bouchet, L., et al. 1993, ApJ, 407, 739
Callanan, P. J., Charles, P. A., Honey, W. B., & Thorstensen, J. R. 1991, MNRAS, 259, 395
Corbel, S., Fender, R. P., Durouchoux, P., Sood, R. K., Tzioumis, A. K., Spencer, R. E., & Campbell-Wilson, D. 1997, in Proc. 4th Compton Symposium, ed. C. D. Dermer, M. S. Strickman, & J. D. Kurfess, (Woodbury, NY: AIP), 937
Covault, C. E., Grindlay, J. E., & Manandhar, R. P. 1992, ApJ, 388, L65
Cowley, A. P., Crampton, D., & Hutchings, J. B. 1987, AJ, 93, 195
Cowley, A. P., Schmidtke, P. C., Crampton, D., Hutchings, J. B., & Bolte, M. 1991, ApJ, 373, 228
Day, C., Arnaud, K., Ebisawa, K., Gotthelf, E., Ingham, J., Mukai, K., & White, N. 1998, The *ASCA* Data Reduction Guide, technical report, version 2.0 (Greenbelt, Md.: NASA GSFC)
Di Matteo, T., Fabian, A. C., Rees, M. J., Carilli, C. L., & Ivison, R. J. 1999, MNRAS, submitted
Dobrinskaya, J., Liang, E., Luo, C., Sheth, S., & Smith, I. 1997, in X-Ray Imaging and Spectroscopy of Cosmic Hot Plasmas, ed. F. Makino & K. Mitsuda (Tokyo: Universial Academy), 481
Dove, J. B., Wilms, J., & Begelman, M. C. 1997a, ApJ, 487, 747
Dove, J. B., Wilms, J., Maisack, M. G., & Begelman, M. C. 1997b, ApJ, 487, 759
Dove, J. B., Wilms, J., Nowak, M. A., Vaughan, B. A., & Begelman, M. C. 1998, MNRAS, 298, 729
Doxsey, R., Grindlay, J., Griffiths, R., Bradt, H., Johnston, M., Leach, R., Schwartz, D., & Scwartz, J. 1979, ApJ, 228, L67
Ebisawa, K., Ueda, Y., Inoue, H., Tanaka, Y., & White, N. E. 1996, ApJ, 467, 419
Esin, A. A., McClintock, J. E., & Narayan, R. 1997, ApJ, 489, 865
Fender, R. P., & Hendry, M. A. 1999, MNRAS, in press
Fender, R. P., Spencer, R. E., Newell, S. J., & Tzioumis, A. K. 1997, MNRAS, 286, L29
Fender, R. P., et al. 1999, ApJ, 519, L165
Grabelsky, D. A., et al. 1995, ApJ, 441, 800
Grebenev, S. A., Syunyaev, R., Pavlinsky, M. N., & Dekhanov, I. A. 1991, Soviet Astron. Lett., 17, 413
Grindlay, J. E. 1979, ApJ, 232, L33
Hannikainnen, D. C., Hunstead, R. W., Campbell-Wilson, D., & Sood, R. K. 1999, A&A, in press
Hjellming, R. M., & Johnston, K. J. 1988, ApJ, 328, 600
Ichimaru, S. 1977, ApJ, 214, 840
Ilovaisky, S. A., Chevalier, C., Motch, C., & Chiappetti, L. 1986, A&A, 164, 671
Imamura, J. N., Kristian, J., Middleditch, J., & Steiman-Cameron, T. Y. 1990, ApJ, 365, 312
Jahoda, K., Swank, J. H., Giles, A. B., Stark, M. J., Strohmayer, T., Zhang, W., & Morgan, E. H. 1996, in EUV, X-Ray, and Gamma-Ray Instrumentation for Astronomy VII, ed. O. H. Siegmund (Bellingham, WA: SPIE), 59
Jahoda, K., et al. 1999, in preparation
Jung, G. V. 1989, ApJ, 338, 972
Kazanas, D., Hua, X.-M., & Titarchuk, L. 1997, ApJ, 480, 280
Kitamoto, S., Tsunemi, H., Miyamoto, S., & Hayashida, K. 1992, ApJ, 394, 609
Lampton, M., Margon, B., & Bowyer, S. 1976, ApJ, 208, 177
Levine, A. M., Bradt, H., Cui, W., Jernigan, J. G., Morgan, E. H., Remillard, R., Shirey, R. E., & Smith, D. A. 1996, ApJ, 469, L33
Lochner, J., & Remillard, R. 1997, ASM Data Products Guide, version dated 1997 August 27[8]
Magdziarz, P., & Zdziarski, A. A. 1995, MNRAS, 273, 837
Makishima, K., et al. 1996, PASJ, 48, 171
Méndez, M., & van der Klis, M. 1997, ApJ, 479, 926
Miyamoto, S., Kimura, K., Kitamoto, S., Dotani, T., & Ebisawa, K. 1991, ApJ, 383, 784
Miyamoto, S., Kitamoto, S., Iga, S., Hayashida, K., & Egoshi, W. 1995, ApJ, 442, L13
Miyamoto, S., Kitamoto, S., Iga, S., Hayashida, K., & Terada, K. 1994, ApJ, 435, 398
Morrison, R., & McCammon, D. 1983, ApJ, 270, 119
Motch, C., Ilovaisky, S. A., Chevalier, C., & Angebault, P. 1985, Space Sci. Rev., 40, 219
Motch, C., Ricketts, M. J., Page, C. G., Ilovaisky, S. A., & Chevalier, C. 1983, A&A, 119, 171
Narayan, R. 1996, ApJ, 462, 136
Narayan, R., Kato, S., & Honma, F. 1997, ApJ, 476, 49
Nørgaard-Nielsen, H. U., Budtz-Jørgensen, C., Westergaard, N. J., & Schnopper, H. W. 1994, A&A, 284, 705
Nowak, M. A., Wilms, J., & Dove, J. B. 1999, ApJ, 517, in press (Paper II)
Pooley, G. G., Fender, R. P., & Brocksopp, C. 1999, MNRAS, 302, L1
Poutanen, J., Krolik, J. H., & Ryde, F. 1997, MNRAS, 221, 21p
Predehl, P., Bräuninger, H., Burkert, W., & Schmitt, J. H. M. M. 1991, A&A, 246, L40
Remillard, R. A., & Levine, A. M. 1997, in All-Sky X-Ray Observations in the Next Decade, ed. N. Matsuoka & N. Kawai (Tokyo: Riken), 29
Rothschild, R. E., et al. 1998, ApJ, 496, 538
Shakura, N. I., & Sunyaev, R. 1973, A&A, 24, 337
Sood, R., & Campell-Wilson, D. 1994, IAU Circ. 6006
Steiman-Cameron, T. Y., Imamura, J. N., Middleditch, J., & Kristian, J. 1990, ApJ, 359, 197
Tanaka, Y., & Lewin, W. H. G. 1995, in X-Ray Binaries, ed. W. H. G. Lewin, J. van Paradijs, & E. P. J. van den Heuvel (Cambridge: Cambridge Univ. Press), 126
Toor, A., & Seward, F. D. 1974, AJ, 79, 995
Trudolyubov, S., et al. 1998, A&A, 334, 895
Turner, M. J. L., et al. 1989, PASJ, 41, 345
Ueda, Y., Ebisawa, K., & Done, C. 1994, PASJ, 46, 107
Zdziarski, A. 1999, in ASP Conf. Proc. 161, High-Energy Processes in Accreting Black Holes: Observational and Theoretical Advances Due to Ongoing Space Missions, ed. J. Poutanen & R. Svensson (San Francisco: ASP), in press
Zdziarski, A. A., Poutanen, J., Mikołajewska, J., Gierliński, M., Ebisawa, K., & Johnson, W. N. 1998, MNRAS, 301, 435
Życki, P. T., Done, C., & Smith, D. A. 1998, ApJ, 496, L25

[8] The ASM Data Products Guide is available on the World Wide Web at http://heasarc.gsfc.nasa.gov/docs/xte/asm_products_guide.html.